NANO-PETROPHYSICS OF THE MARCELLUS FORMATION IN PENNSYLVANIA, USA

by:

Christina Muñoz

Presented to the Faculty of the Graduate School of

The University of Texas at Arlington in Partial Fulfillment

of the Requirements for the Degree of

MASTER OF SCIENCE IN GEOLOGY

THE UNIVERSITY OF TEXAS AT ARLINGTON

May 2019

Acknowledgements

I would like to thank Dr. Qinhong Hu for his mentorship during my graduate career at UTA. The research achievements done by his group has contributed greatly for better understanding unconventional reservoirs. I appreciate being given the chance and taking part of the group. I would also thank Dr. Wickham and Bill Moulton for all their guidance and for having served on my committee. Your advice and mentorship towards my academic and professional career have been truly appreciated.

I would like to thank Pennsylvania Department of Conservation and Natural Resources for providing core samples for this research project. This project would not be possible without the preservation of the core and careful distribution for research purposes, especially with the assistance from John Neubaum and Lindsey Ditzler with core and data retrieval. A special thanks are also extended to DrillingInfo for providing complimentary production information and figures for this study. I am eternally grateful for my grandmother, Enriqueta Cuevas, for supporting me even in the afterlife. The unconditional love and support from my parents, Nemesio and Maria Munoz, your sacrifices had led to this moment. My brother, David Munoz, for his support and service to this country. Steven for uprooting me and opening my eyes to the oil and gas wonders from Texas to Wyoming. Rebekah, Cathina, Erin, thank you for staying by my side! I would like to thank my supportive family and friends for allowing me to chase life, fail, and persevere; for without this, I wouldn't be me.

April 26, 2019

Abstract

NANO-PETROPHYSICS OF THE MARCELLUS FORMATION IN PENNSYLVANIA, USA

Christina Munoz, MS

University of Texas at Arlington, 2019

Supervising Professor: Qinhong Hu

Characterizing unconventional shale reservoirs consisting of nano-size pores and pore networks are complicated due to their complex geometric structure and restrictive fluid transport abilities. Technological advancements with the use of multiple laboratory techniques for unconventional shale characterization has played key roles in determining their petrophysical properties with greater understanding and accuracy. Successful assessment of reservoir properties can be achieved by the measurement of porosity, permeability, pore size distribution, total organic carbon content, mineralogy, thermal maturity, wettability, tortuosity, with an understanding of the dispositional environments.

The Marcellus covers as much as six states and occurs as deep as 9000 feet below the surface indicating a large potential and storage capacity for natural gas. Despite the Marcellus being the top shale gas producer in the United States it's also characterized by low porosity and permeability resulting in low-yields with declining production rates in some wells. In efforts to increase production or higher-yielding well completions in the shale, a greater understanding of the reservoir's petrophysical properties are essential for evaluation.

This study will focus on the evaluation of nano-petrophysical properties of the Marcellus and underlying Utica that will provide additional information to the behavior of unconventional shale formations of the Appalachian basin, Pennsylvania. A series of experimental methodologies will be performed on samples gathered from five wells and two outcrops of the Marcellus and Utica formations in Pennsylvania. Analyses to be performed on samples include vacuum saturation, wettability/contact angle, x-ray diffraction (XRD), geochemistry, liquid pycnometry, mercury injection capillary pressure (MICP), imbibition and vapor absorption, and well-log analyses. Observations are then used to determine pore geometry and connectivity, migration, and storage characteristics within the Marcellus and Utica formations in the Appalachian basin, Pennsylvania. This will contribute to a better understanding of reservoir properties leading to the enhancement of well stimulation and completion methodologies for increased fluid migration and potentially increased production.

Table of Contents

List of Illustrations

List of Tables

List of Equations

Chapter 1 – Introduction

The Marcellus located in the Appalachian Basin has been a one of the most prolific natural gas producing formations in the United States. The formation has been known for some time, as was described by J. Hall in 1839, yet still acts as an emerging hydrocarbon producer in the Northeast U.S. The Marcellus is an unconventional Middle Devonian organic-rich shale located in the Appalachian basin of the Northeast U.S. that continues to challenge researchers due to horizontal drilling and hydraulic fracturing techniques and methods required for economical production. In 2013, the United States EIA estimated that 4644 trillion cubic feet of gas-in-place could potentially exist in shale gas formations in the U.S. (EIA, 2013). As of January 2015, approximately 10 Trillion cubic feet (Tcf) of natural gas have been produced from Marcellus wells, accounting for one third of the nation's yearly gas consumption (Male, 2016).

In the 1930s, the oil and gas industry noticed gas "pockets" in the formation while drilling for the underlying Oriskany Sandstone (Harper, 2008). During the energy crisis of 1973 the U.S Department of Energy founded a cooperative program called the Eastern Gas Shales Project (EGSP) that spanned the Appalachian basin in Pennsylvania in which several samples have been collected and analyzed from the Marcellus are discussed in this study. Organic rich shales, like the Marcellus, produce large amounts of hydrocarbons as unconventional reservoirs which are classified as deep gas, tight gas, gas-containing shales (Belvalkar, 2010). Due to technological advancements, characterization methods are performed to allow researchers to better understand

properties of tight unconventional reservoirs. In this study petrophysical methods including mercury injection capillary pressure (MICP), wettability/contact angle, x-ray diffraction (XRD), TOC and pyrolysis, vacuum saturation, fluid imbibition and vapor absorption, are performed to calculate and observe the nano-petrophysical characteristics and formation evaluation of the Marcellus. These methods are tested and used to quantify porosity, pore size distribution, and pore connectivity of the Marcellus and Utica shales.

1-1 Objectives of Study

Shale gas plays are assessed in terms of depositional environment, thickness, organic geochemistry, thermal maturity, mineralogy, porosity and permeability (Rezaee, 2015). The Marcellus Shale is the lowermost formation in the Hamilton Group which is comprised of three formations: The Tully Limestone, Mahantango Shale, and ultimately the Marcellus. The Marcellus consists of thinly laminated black to grayish black siliceous mudstones. Depositional and diagenetic processes are controlling factors of the significant lithological heterogeneity across the basin (EIA, 2017). Total Organic Carbon (TOC) content in the Marcellus formation ranges from less than 1% to 20% (Nyahay et al., 2007). Previous studies show that the Marcellus have wide calculated permeability ranges from 5-50 μd to 20-60 nD (Soeder et al., 1986; Heller et al., 2014).

Pennsylvania's natural gas production reached a new high of 15 billion cubic feet per day (Bcfd) in October 2017 as shown in Figure 1-1. The state of Pennsylvania alone currently accounts for 19% of the natural gas production in the U.S. A large amount of

natural gas production is from the Marcellus shale formation, 76% of which currently produced in Pennsylvania. Oil reserves in the Marcellus are estimated to be of 143 million barrels (MMbbls) (EIA, 2017). The mean well is expected to produce 3.62 Bcf over its 25-year life span and dominated flow boundary time of 3.9 years in the Marcellus (Male, 2016).

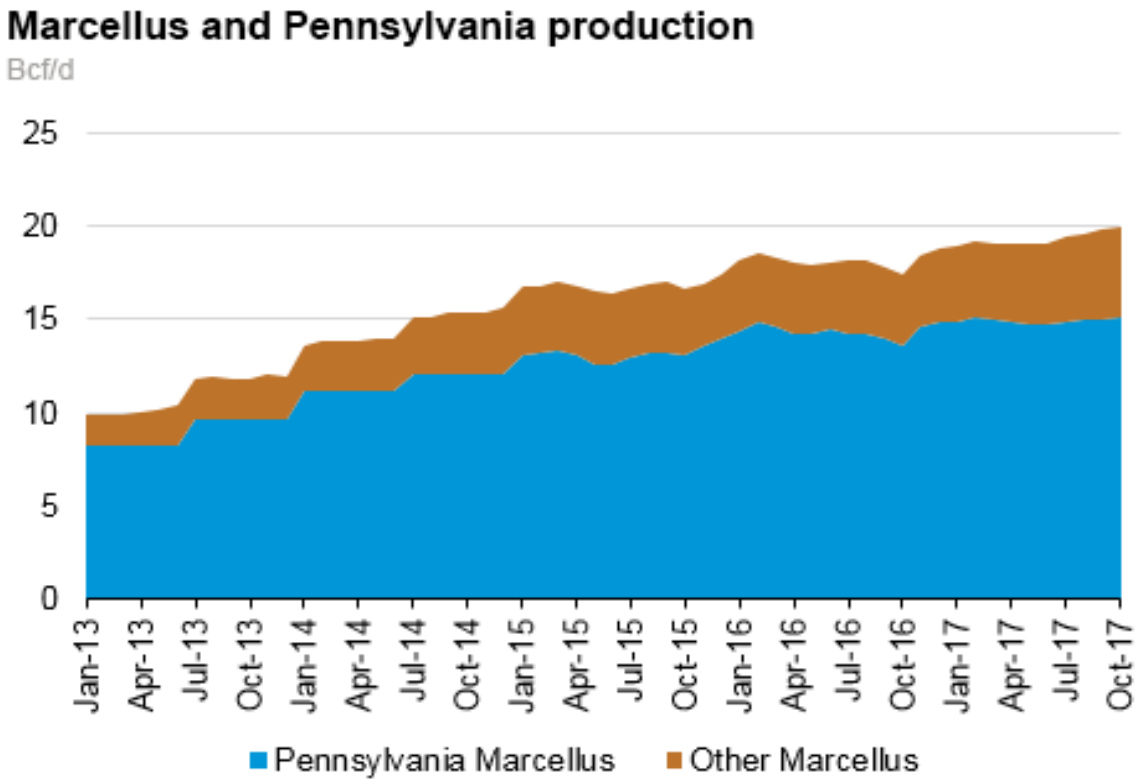

Figure 1-1: Marcellus and Pennsylvania production (From U.S. Energy Information Administration, 2018).

Decline curves have been observed and altered to predict recovery rates produced by increased technological advancements and recovery completion methods. The objective of this study is to correlate available core mineralogical characteristics and petrophysical techniques that influence economic production from various intervals in the Marcellus in Pennsylvania. Utilizing reservoir characterization techniques to quantify nano-petrophysical properties of tight shale play will broaden our understanding of the Marcellus. Altering fracking networks or re-fracking is complicated and costly but in concurrence with reservoir characterization will contribute greatly to studying unconventional reservoirs behaviors. Studying the pore network and edge accessible characteristics of the Marcellus will contribute to better understanding fluid flow and hydrocarbon migration in tight shales.

1-2 Hypothesis

Pore structure plays an essential role in fluid migration, therefore quantifying the nano-petrophysical characteristics of tight gas shale reservoirs will be performed on the Marcellus. This study will provide an analysis on the nano-petrophysical characteristics that are linked to porosity and permeability values in the Marcellus.

A variety of testing methods will be performed on five wells and two outcrops, sampled from the Marcellus and Utica formations, to study the distinctive relationship between pore size distribution utilizing MICP with pore connectivity from imbibition and vapor absorption experiments coupled with geochemical analyses. I propose that TOC variations and mineralogical characteristics affect pore size distribution and connectivity

that make up the Marcellus. In addition, bulk density calculations from vacuum saturation, liquid pycnometry, MICP analyses will be correlated. Mineralogical content will be plotted with TOC% to determine any potential trends that will affect porosity and permeability results.

Chapter 2 - Geologic Setting

The Marcellus and Utica formations are black organic-rich shales located in the Appalachian basin (Figure 2-1). This ancient foreland basin has a large potential and storage capacity for natural gas formed from a series of complex geologic events. The northeast-southwest trending basin is roughly 2,050 km long with an area of 536,000 km^2 that extends from southern Quebec in Canada to Alabama in the U.S. (Ettensohn, 2008). At about 1.3 to 1.1 billion years ago (bya), the Laurentian crustal block forming the North America craton collided with additional microplates to become Rodinia. The basin began to accumulate along a passive margin initiated by the breakup of Laurentia with Rodinia. The Iapetus Ocean and Rome trough were then created by the rifting event in the late Precambrian about 750 million years ago (mya) that initially started the Appalachian deformation and sedimentation cycles (Shultz, 1999).

During the Late Ordovician, a volcanic arc collided with the North American plate to cause the Taconic orogeny at roughly 440 – 480 mya ago. Consequently, thrusting material from the arc and floor of the Iapetus Ocean onto the North American plate

margin. This was the first of three principle orogenies that helped build the Appalachian Mountain range. As mountain buildup occurred, clastic sediments deposited onto the plate margin overlying clay and silt sediments causing an additional subsidence. This led to the development of the Appalachian basin, an elongated foreland basin formed west of the Taconic Mountains during the Late Ordovician. Sediments depositing in the basin about 450 mya ago would consolidate and form to what is currently known as the Utica Formation. The Taconic orogeny would continue into the Early Silurian with erosion occurring in the Late Silurian.

In the Early to Middle Devonian, marine shelf conditions continued into the basin after a major detrital influx of sediment formed westward into the foreland sea building what is known as the Catskill delta. During the Middle to Late Devonian the Acadian orogeny occurred at roughly 469 – 316 mya created the Acadian mountains (highlands) east of Pennsylvania (Figure 2-2). As uplift continued, sediment deposition into the basin (Figure 2-3) created asymmetrical wedge-shaped deposits due to difference in subsidence and sedimentation rates at both ends of the basin (Ettensohn, 1985).

As the deformation of the Acadian highlands and uplift of the Taconic mountains occurred this generated a vast amount of sediment deposition contributing to the growth of the basin resulting in lower amounts of available oxygen. Large volumes of course-grained sediment poured into the western trough area (Figure 2-4), as in the west, adjacent to the North American craton, the Devonian fine-grained sediments and organics settled deeper into the basin (Shultz, 1999). The organic-rich shales, such as the Marcellus, were deposited in the foreland basin Middle Devonian about 390 mya in

relatively deep anoxic waters (Harper, 1999). A generalized stratigraphic column (Figure 2-5) focused in Pennsylvania highlighting both the Marcellus and Utica formations deposited in the Appalachian basin.

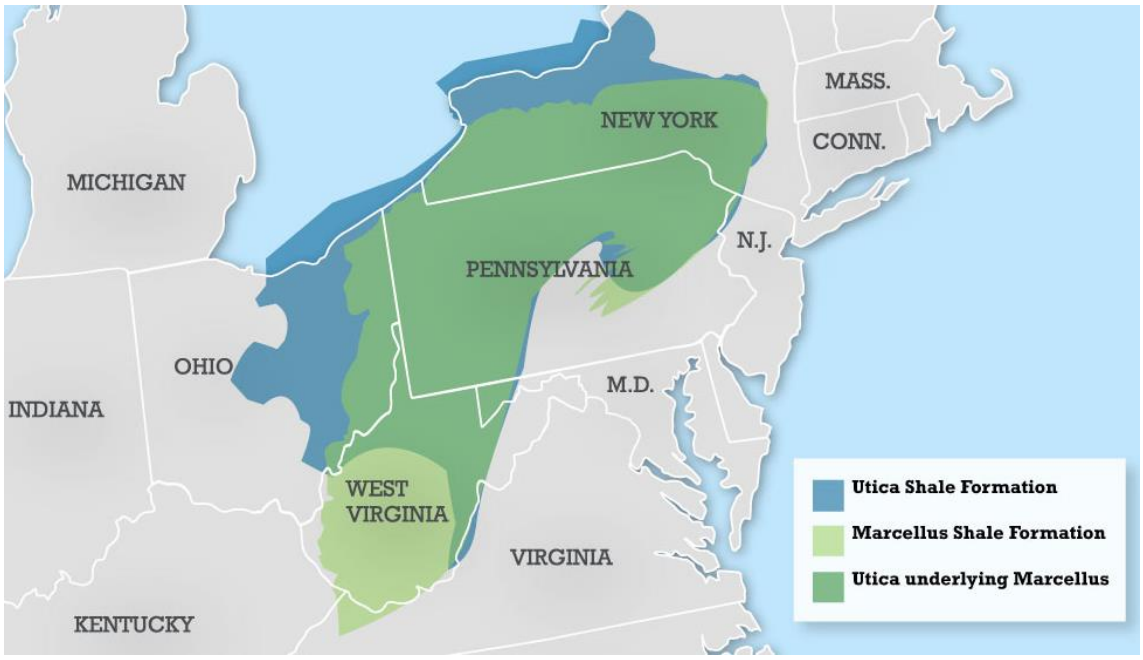

Figure 2-1: Boundaries of the Marcellus and Utica formations (from the Marcellus Shale Coalition, 2018).

Figure 2-2: Middle to Late Devonian (385 mya) Paleogeography (from Blakey, 2011).

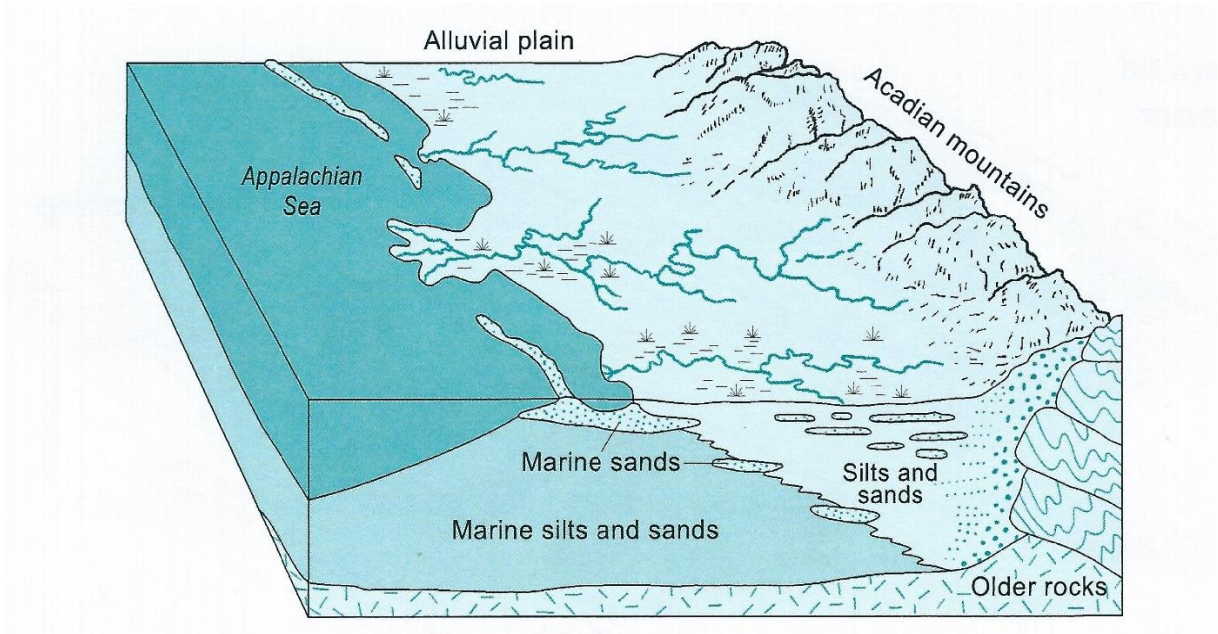

Figure 2-3: Illustration of migrating environments of deposition in the Late Devonian (from Barnes, 2014).

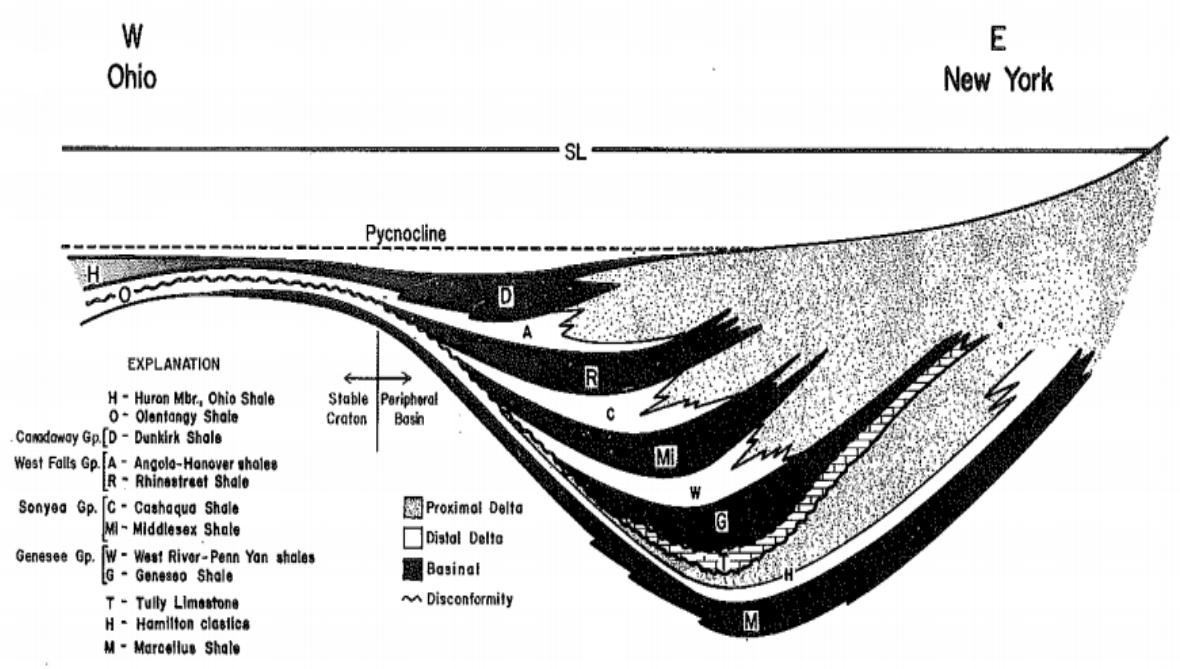

Figure 2-4: Schematic diagram of the proximal-delta-distal-delta and basinal facies for the Middle and Upper Devonian Catskill Delta from Ohio to New York (from Ettensohn, 1985).

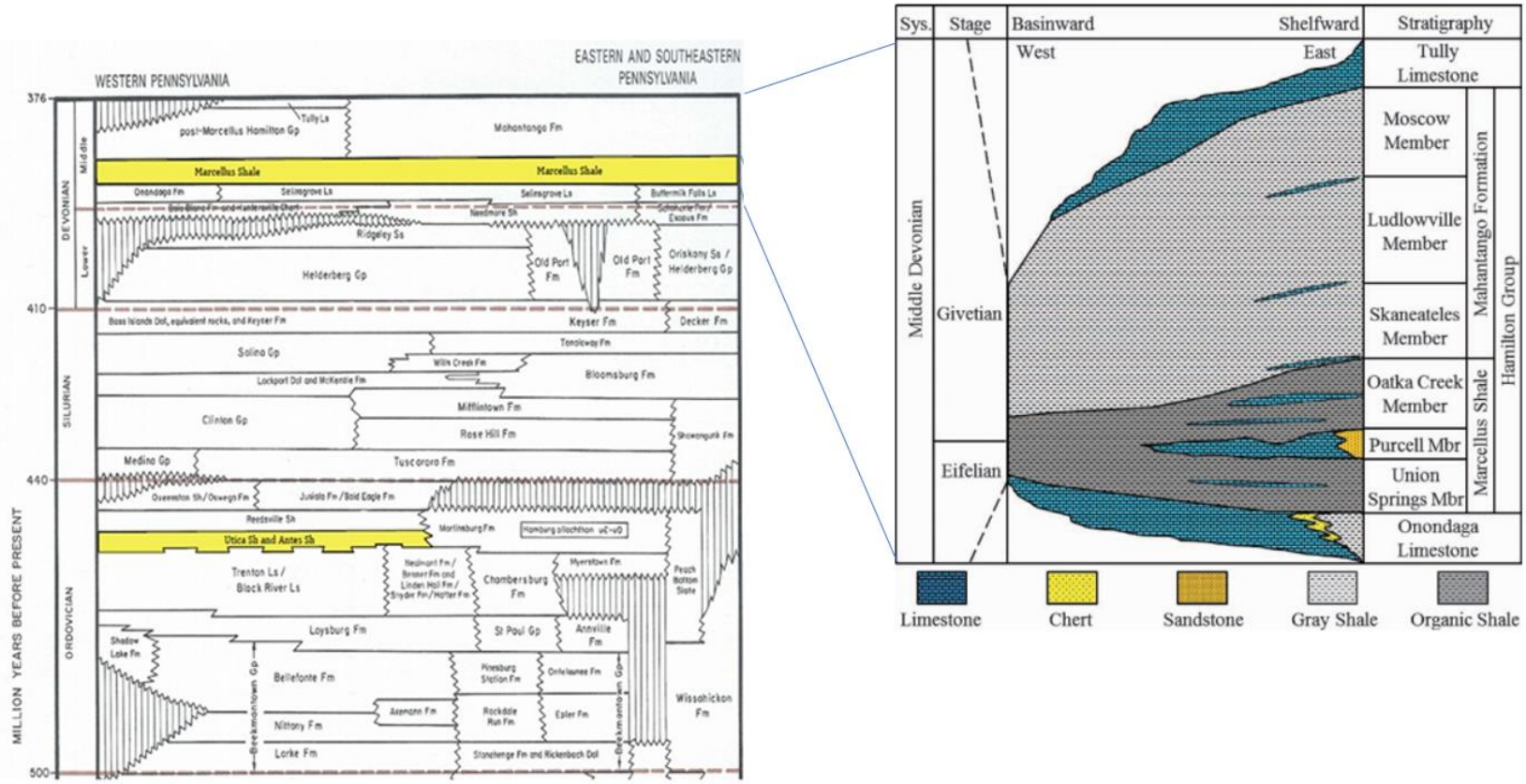

Figure 2-5: Generalized stratigraphic chart of the Appalachian basin. The Marcellus is divided into two members by the Purcell limestone, the Upper Marcellus, known as Oatka Creek, and the Lower Marcellus known as Union Springs (modified from Shultz 1999 and Wang, 2013).

Chapter 3 - Methods

3-1 Sample Procurement and Preparation

Core samples were obtained from the Pennsylvania Department of Conservation and Natural Resources (DCNR). Samples were taken from five wells, EGSP #2, EGSP #5, Bald Eagle 2015, Bennet, and CLIO35_0385, ranging from central to western Pennsylvania. These wells were chosen for their higher core recovery rates in the Marcellus sections and desired locations in Pennsylvania. In addition to core samples, outcrop samples were obtained from two shallow dipping Marcellus outcrops (Figures 3-1 and 3-2) in central Pennsylvania. A total of 17 (Table 3-1) samples were obtained between the five wells and two outcrop locations for this study (Figure 3-3). The DCNR provided additional analytical data on the wells discussed in this study. Available data donated to the DCNR by Weatherford Laboratories for the Bennet Well include TOC, pyrolysis, XRD, vitrinite reflectance, and kerogen type.

Figure 3-1: Hootenanny Camp Borrow Pit outcrop. Cold Springs Road, Huntingdon, PA. Shallow-dipping Marcellus Shale (Oatka Creek Member) revealing excellent jointing characteristics.

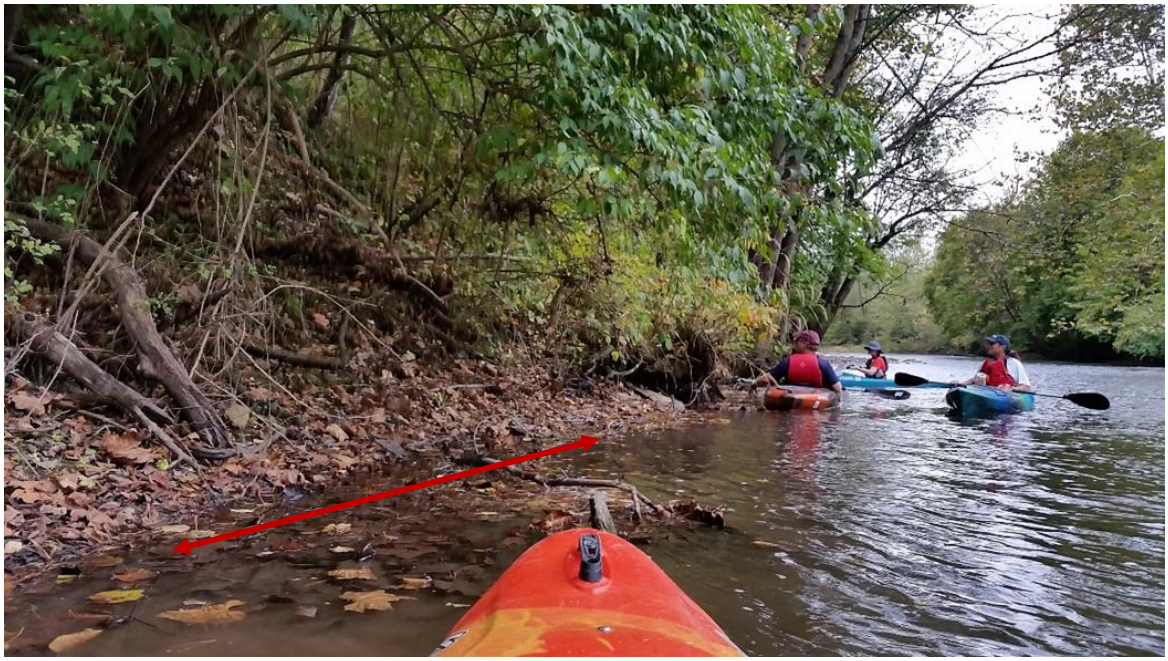

Figure 3-2: Outcrop in the Bald Eagle Creek southwest Milesburg, PA.

Table 3-1 Sample locations in Pennsylvania

Well/Outcrop Name	Sample Depth (Ft)	Sample Name	Formation	County	Surface Lat	Surface Long
EGSP #2	7378	EGSP-7378	Marcellus	Alleghny	40.383194	-80.241667
	7418	EGSP-7418				
	7461	EGSP-7461				
	7495	EGSP-7495				
EGSP #5	4020	EGSP-4020		Lawrence	41.09202	-80.281696
	4036	EGSP-4036				
	4081	EGSP-4081				
	4095	EGSP-4122				
BALD EAGLE 2015 / HUNTER'S RUN	248	BE-248		Centre	41.05355	-77.619509
	289	BE-289				
	342	BE-342				
BENNET	8299	BNT-8299		Sullivan	41.3520859	-76.5154958
	8300	BNT-8300				
	8327	BNT-8327				
Bald Eagle Creek Outcrop	Surface	BEC Outcrop		Centre	40.96204	-77.7491
Hootenanny Camp Borrow Pit	Surface	HNY Outcrop		Huntingdon	40.554536	-77.96383
CLIO35_0385	240	CLO-240	Utica	Clinton	41.05822	-77.42572

A list of obtained samples and performed experiments are shown in Table 3-2. Vacuum saturation, fluid pycnometry, XRD, TOC, pyrolysis, and contact angle were performed on all samples. Imbibition and vapor absorption were carried out on samples with large enough sample size for testing. MICP was performed on samples with larger porosity and TOC percentages (Table 3-3): EGSP-7461, EGSP-7495, EGSP-4036, EGSP-4081, EGSP-4122, EGSP-8299, EGSP-8327, and CLO-240. Such methods are used to quantify porosity, pore size distribution, and pore connectivity of the porous media and results are compared with respect to geochemical characteristics. Sample and microscopic images (Figure 3-4) were taken prior to samples being cut into $1cm^3$ cubes

using a Hi-Tech Diamond saw (Figure 3-5). Two cubes were labeled T (top), B (bottom) faces (Figure 3-6) for imbibition and vapor absorption testing including 3 cubes X, Y, Z for vacuum saturation and MICP. For contact angle and wettability experiments, thin (2mm $\times$ 1cm $\times$ 1cm) slaps were cut from additional $1cm^3$ cubes. The exposed surfaces of the cubes and slabs were polished with sandpaper. The imbibition and vapor absorption cubes were then epoxied at 4 of 6 sides to allow fluid flow in one desired direction. After cubes and slabs were cut, the remaining sample mass provided six different size fractions in respective orders of GRI+, size A, GRI (Gas Research Institute), size B, size C, and powder (Table 3-3). Mass of sample size fractions were dependent on the size of the initial sample. Samples were then placed into vials and logged.

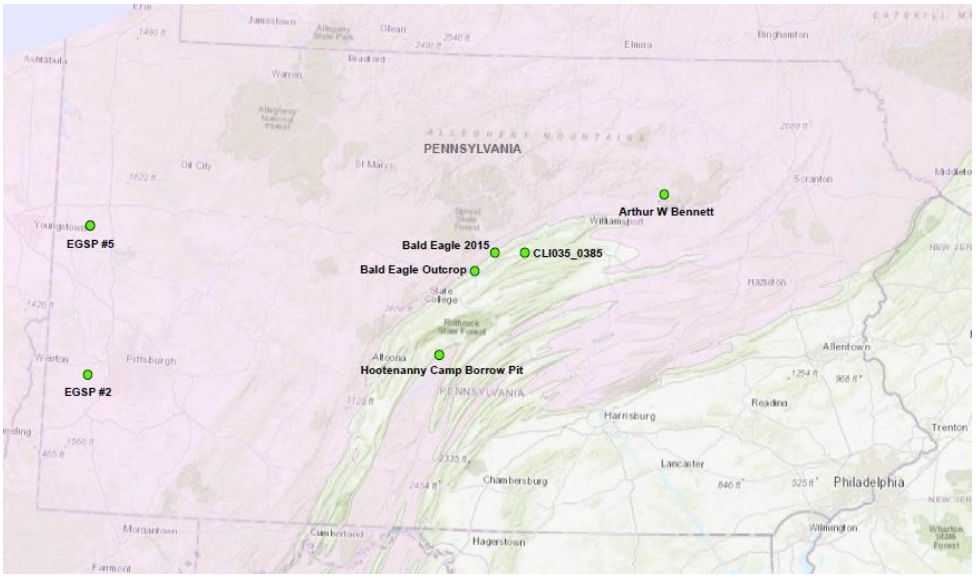

Figure 3-3: Sample locations with the extent of the Marcellus (pink).

Table 3-2: List of experiments performed in this study.

Sample ID	Vacuum Saturation	Contact angle	XRD	TOC	Pyrolysis	Liquid pycnometry	MICP	Imbibition	Vapor absorption
EGSP-7378	√	√	√	√	√	√		√	√
EGSP-7418	√	√	√	√	√	√			
EGSP-7461	√	√	√	√	√	√	√	√	√
EGSP-7495	√	√	√	√	√	√	√	√	√
EGSP-4020	√	√	√	√	√	√		√	√
EGSP-4036	√	√	√	√	√	√	√		
EGSP-4081	√	√	√	√	√	√	√		
EGSP-4122	√	√	√	√	√	√	√	√	√
BE-248	√	√	√	√	√	√		√	√
BE-289	√	√	√	√	√	√			
BE-342	√	√	√	√	√	√			
BNT-8299	√	√	√	√	√	√	√	√	√
BNT-8300	√	√	√	√	√	√			
BNT-8327	√	√	√	√	√	√	√	√	√
BE-Creek Outcrop	√	√	√	√	√	√		√	√
HNY Outcrop	√	√	√	√	√	√			
CLO-240	√	√	√	√	√	√	√	√	√

Table 3-3: Sample size fractions (g) for each sample discussed in this study (note the names of GRI+ and others are locally used in our research lab).

Sample ID	GRI+ (#8/#12) mass; g	Size A #12/#20 mass; g	GRI (#20/#35) mass; g	Size B (#35/#80) mass; g	Size C (#80/#200) mass; g	Powder (<#200) mass; g
EGSP-7378			1.63	21.81	18.34	5.56
EGSP-7418	10.59	17.36	15.708	10.81	7.38	1.2
EGSP-7461		16.85	24.418	25.76	10.2	2.3
EGSP-7495	26.41	38.26	21.635	28.04	15.07	7.53
EGSP-4020	7.41	16.94	17.158	19.43	4.63	2.06
EGSP-4036	25.15	45.48	31.07	27.68	8.82	3.59
EGSP-4081	9.86	31.05	21.802	28.14	11.21	2.55
EGSP-4122		8.54	12.549	15.75	7.86	3.94
BE-248	34.996	43.785	21.65	23.449	11.301	4.697
BE-289	27.34	33.32	20.134	28.83	13.87	3.67
BE-342	14.93	24.01	16.349	17.23	8.36	1.67
BNT-8299	9.44	19.86	15.159	17.2	7.77	2.65
BNT-8300	7.07	15.04	9.971	11	4.36	1.658
BNT-8327	8.77	23.3	10.559	13	8.4	2.48
BEC-Outcrop	30.76	32.4	14.548	18.74	12.01	2.74
HNY-Outcrop	38	37.22	20.341	20.98	10.74	3.63
CLO-240			24.654	30.99	15.24	5.56


Marcellus Shale
EGSP #2
PA EGSP-7378
7378.15 ft
Allegheny Co., PA

(A)


Marcellus Shale
EGSP #2
PA EGSP-7418
7418.10 ft
Allegheny Co., PA

(B)


Marcellus Shale
EGSP #2
PA EGSP-7461
7461.00 ft
Allegheny Co., PA

(C)

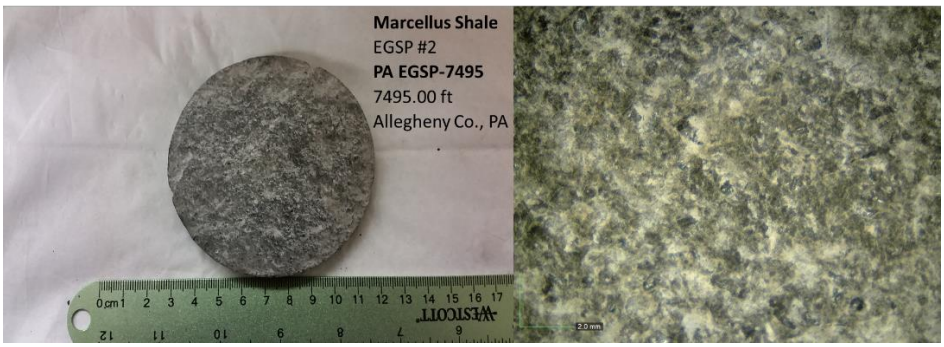
Marcellus Shale
EGSP #2
PA EGSP-7495
7495.00 ft
Allegheny Co., PA

(D)

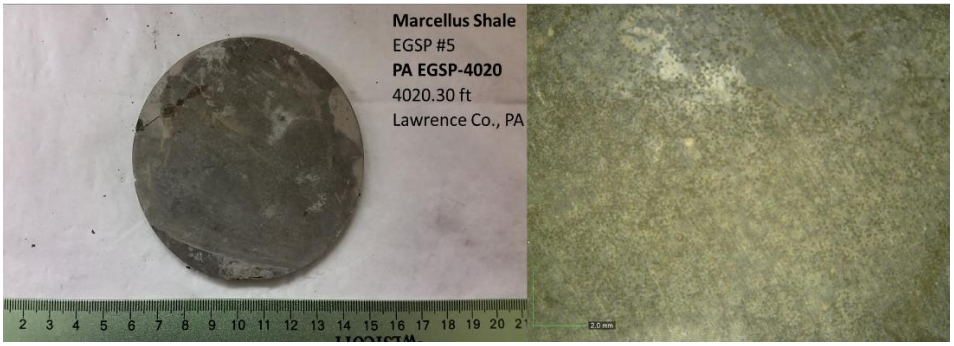
Marcellus Shale
EGSP #5
PA EGSP-4020
4020.30 ft
Lawrence Co., PA

(E)


Marcellus Shale
EGSP #5
PA EGSP-4036
4036.90 ft
Lawrence Co., PA

(F)

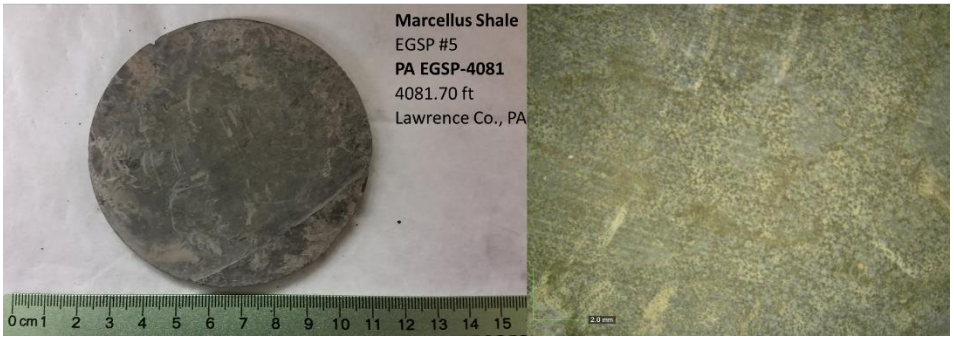
Marcellus Shale
EGSP #5
PA EGSP-4081
4081.70 ft
Lawrence Co., PA

(G)

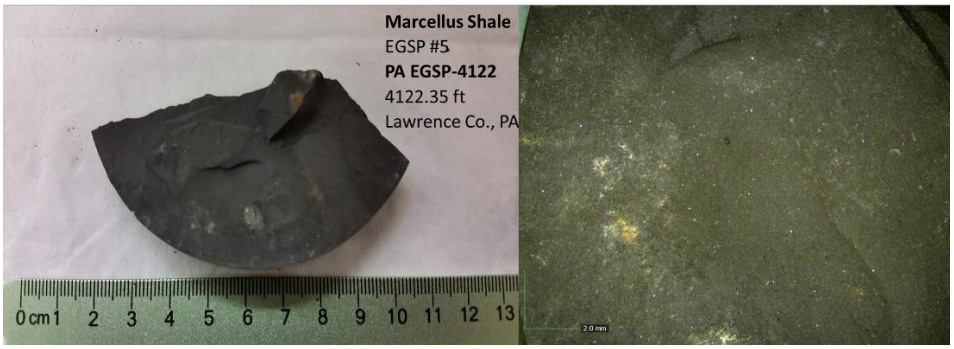
Marcellus Shale
EGSP #5
PA EGSP-4122
4122.35 ft
Lawrence Co., PA

(H)

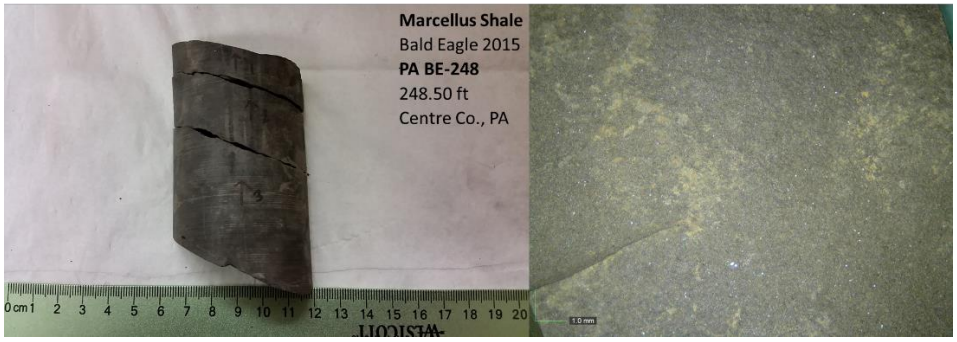
Marcellus Shale
Bald Eagle 2015
PA BE-248
248.50 ft
Centre Co., PA

(I)

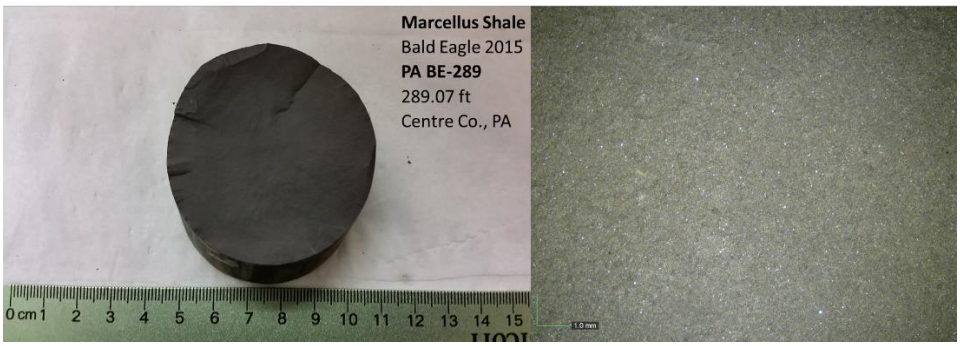
Marcellus Shale
Bald Eagle 2015
PA BE-289
289.07 ft
Centre Co., PA

(J)

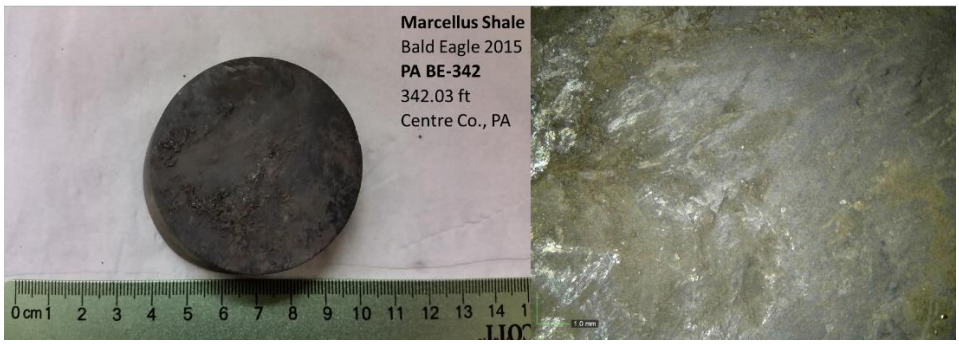
Marcellus Shale
Bald Eagle 2015
PA BE-342
342.03 ft
Centre Co., PA

(K)

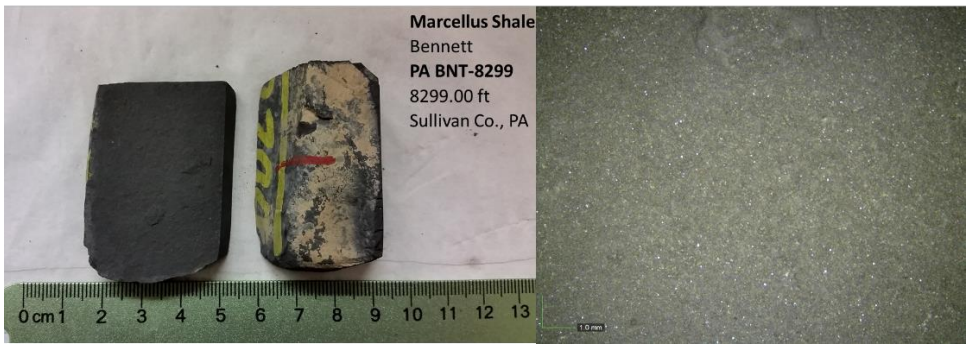
Marcellus Shale
Bennett
PA BNT-8299
8299.00 ft
Sullivan Co., PA

(L)

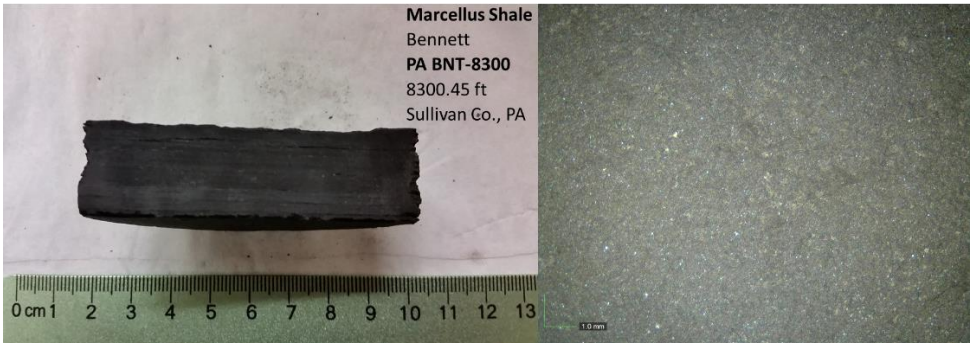
Marcellus Shale
Bennett
PA BNT-8300
8300.45 ft
Sullivan Co., PA

(M)

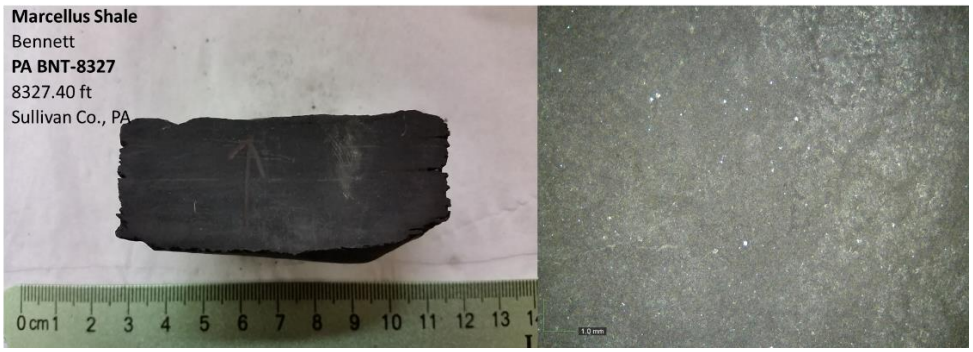
Marcellus Shale
Bennett
PA BNT-8327
8327.40 ft
Sullivan Co., PA

(N)


Marcellus Shale
Bald Eagle Outcrop
BE-Creek Outcrop

(O)

(P)

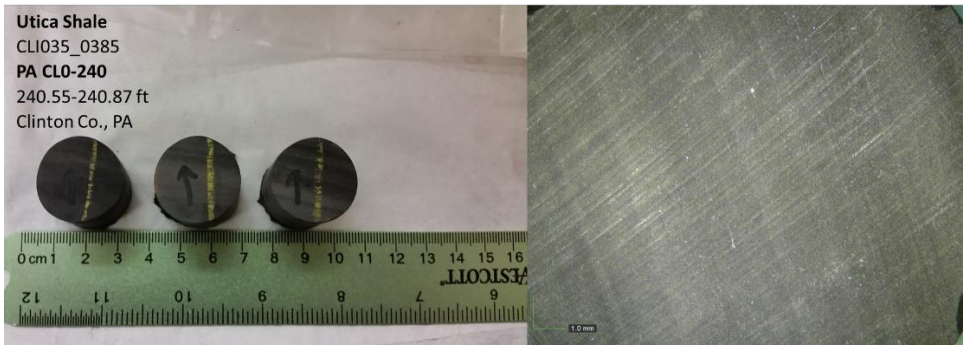

(Q)

Figure 3-4: Microscopic and hand-sample images prior to cutting.

Figure 3-5: Hi-Tech Diamond saw used to cut samples into cubes.

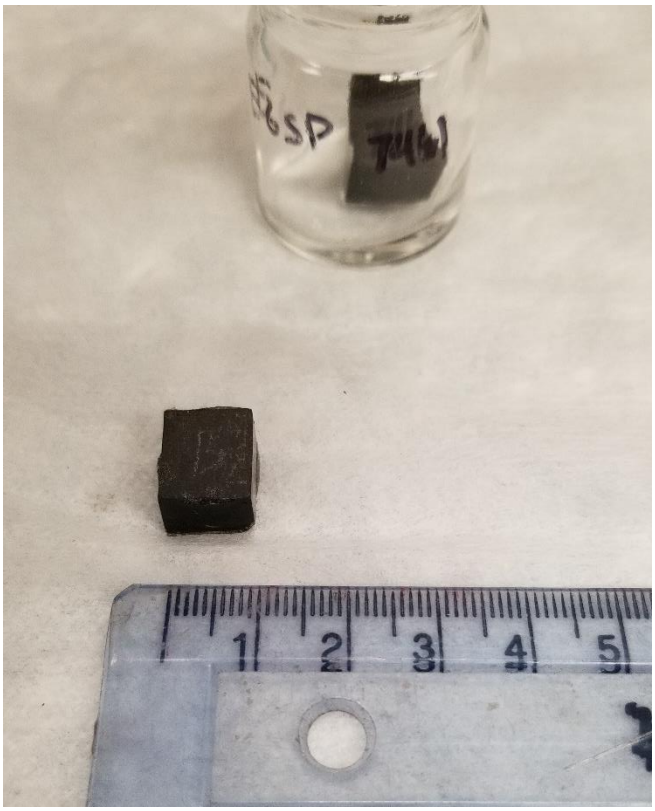

Figure 3-6: Sample image of EGSP-7461 cut down to 1 cm cube size.

3-2 Vacuum Saturation

Vacuum saturation, followed with the Archimedes' displacement method, is used to investigate the pore structure of the porous medium. This method can also be utilized to study the edge-only accessible porosity distribution of poorly connected and/or low porosity rocks. The apparatus consists of a chamber connected to a vacuum pump, compressed gas (CO_2) cylinder, and fluid reservoir. The purpose of this method is to evacuate the air in the edge-accessible pores of the samples sealed in the chamber for several CO_2 cycles, since CO_2 is better dissolved in DI water than air, subsequently leading to the evacuation of the edge-only connected pores. Samples are weighed prior to and after completion of testing to measure the total mass of saturated fluid in the samples thereby calculating the accessible pore volume and sample densities.

Procedure for Vacuum Saturation

Irregular samples, core plugs, and 1cm cubes were used for sample testing. Due to the available mass of samples included in this study, irregular samples for BE-289, BE-342, BNT-8299, BNT-8300, BNT-8327 were tested and all 1cm cube samples were tested except for the HTNY outcrop. Prior to testing the samples dimensions, initial air-dry weight, 60^{o}C oven dry weight were measured and recorded. Irregular samples were saturated in DI water only and cubes were saturated in DI water, tetrahydrofuran (THF), and DT2 (2:1 ratio in volume of n-decane and toluene) used as a substitution for oil to determine the wettability of the sample surface towards oil.

Sample Evacuation

Dried samples were placed into the chamber using custom made plastic or aluminum sample racks depending on the fluid type. Drawings and images were taken to secure sample location in trays, samples were labeled with lead for identification purposes as well. Once samples were secured in the chamber, the lid was attached and tightened using flat washers and wing nuts (Figure 3-7). The valve connected to the fluid reservoir is turned to the closed position and the three-way valve connecting to the vacuum, compressed gas, and sample chamber is opened toward the vacuum line. The pressure gauge was connected, and the vacuum pump turned on. Once the experiment was initiated, a timer was set. The pressure should get down as low as 0.05 Torr in 30 minutes. The pressure drawdown was recorded with respect to time. Once the pressure was achieved the chamber was evacuated for at least 8 (12-18 for overnight) hours for shale samples of 1-2 cm linear length. Lowest achieved pressure during vacuum and duration under vacuum were recorded.

Introducing CO_2 to displace residual air

The 3-way valve is turned open toward the pressurized gas line and the vacuum pump was turned off with the gas regulator turned in the closed position. The regulator valve is slowly turned until the pressure begins to rise until the gauge reads 50 psi. The 3-way valve is closed to prevent leakage through the CO_2 hose. CO_2 is released into the chamber for 30 minutes, vacuum is pulled for 2 hours, until pressures approach 0.05 Torr. CO_2 is released for 30 minutes, and then vacuum is pulled for 8 hours (12-18 hours overnight).

Fluid Introduction

Once samples have been sufficiently evacuated samples are fully immersed in the chamber with desired fluid. Samples are immersed and CO_2 is applied to pressurize fluid into pore spaces. CO_2 introduction steps are repeated, and samples are left under pressure for at least 8 hours (12-18 hours overnight). Once duration has passed, the lid is detached, and excess fluid is removed from the reservoir. Samples are weighed by gently wiping excess fluid using a moist Kimwipe (with the same saturating fluid) before weighing, then re-submerged in the saturating fluid and this process is repeated.

Figure 3-7: Vacuum chamber setup with samples in the chamber to the left

3-3 Wettability and Contact Angle

Wettability quantifies the preferential tendency of a fluid to wet a rock surface in the presence of another fluid (Agbalaka et al., 2008). A porous medium's organic composition and mineralogy alters the wettability state, in turn varies depending on pore size distribution. Different types of fluids are introduced to determine the wettability state of samples discussed in this study. Quantifying wettability is critical in selecting fracturing fluids and ultimately improve recovery rates in low permeable formations.

Procedure for Wettability and Contact Angle

The wettability of the rock sample surfaces was experimented on thin slabs using DI water, 10% tetrahydrofuran (THF), American Petroleum Institute (API) brine, and DT2. Both DI water and API brine are water wetting fluids. API brine, is composed of 8% NaCl and 2% CaCl2 by weight, is used for its high salinity characteristics that of formation water (Crowe, 1969). DT2 is an organic fluid used as a substitution for oil to determine the wettability of the sample surface towards oil. THF is a fluid that has characteristics which is both hydrophilic and hydrophobic. One side of the shale slab sample is used for DI water with its opposite side for API brine, and another slab were used for 10% THF and DT2. These experiments expose tendencies of whether the rock surface is water or oil wet on a millimeter scale. When the fluid spreads on the sample surface, the surface is considered wetting to this fluid and will subsequently have a small contact angle (Figure 3-8). A droplet of fluid is pipetted onto a 2 mm$\times$10 mm$\times$10 mm thin rock slab surface while simultaneously being timed. The SL200KB Optical Contact Angle Meter (Kino

USA) records and measures the contact angle of the droplet on the rock surface of the sample respect to time.

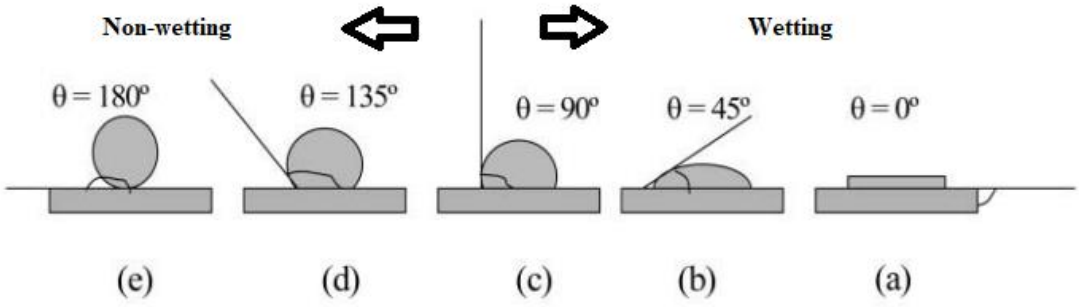

Figure 3-8 Range of contact angles for wetting and non-wetting fluids placed on the surface (modified from Mujika, 2005).

3-4 Mineralogy

XRD analysis were performed with the methods provided in Appendix A – Methods and Procedures for Geochemical Analysis at the Shimadzu Center. XRD was performed on all provided sample depths in this study. Bulk XRD analysis was performed on 17 samples, using a MaximaX XRD-7000 Shimadzu X-ray Diffractometer to characterize their mineral composition and clay content (Rezaee, 2015). Bulk percentages are calculated and plotted on a lithofacies ternary diagram.

3-4 Geochemistry

TOC and Pyrolysis analysis were performed by GeoMark and the methods used are provided in Appendix B – Methods and Procedures for TOC and Pyrolysis Analysis at GeoMark. Pyrolysis and total organic carbon (TOC) percentages were performed on all 17 sample depths in the study. TOC is measured to quantify the amount of organic carbon in a sample. Thermal maturity is determined by the chemical measurement of pyrolysis testing, which is the maximum temperature at the (S2) peak, T_{max}. Kerogen type affects T_{max} values as well as the shape of the pyrolysis peak (Rezaee, 2015).

Data given for pyrolysis testing are S1, S2, S3, and T_{max} with TOC percentages. S1 determines residual hydrocarbons available in the rock. S1 hydrocarbons could be derived from organic molecules that have maturated in the rock or have migrated from another source. S2 measures the remaining hydrocarbon generation potential in the rock. S3 measures, if any, trapped carbon dioxide in the rock. T_{max} measures the highest possible temperature reached during maximum S2 generation.

3-5 Liquid Pycnometry

Liquid displacement is used to calculate bulk density of different sample size fractions in a fluid, as they cannot be worked with vacuum saturation approach. Particle density is calculated from porosity and bulk density by carefully measuring mass and volume. The particle density can be determined by the ratio of bulk density divided by one minus the porosity (Flint, 2002):

$$\rho_p = \rho_b / (1-\phi) \qquad \text{Equation 3-1}$$

Where:

ρ_p = Bulk density (g/cm^3)

ρ_b = Particle density (g/cm^3)

ϕ = Porosity (fraction)

Particle density utilizing pycnometry method is determined by:

$$\rho_p = [\rho_w(W_s-W_a)]/[W_s-W_a)-(W_{sw}-W_w)] \qquad \text{Equation 3-2}$$

Where:

ρ_w = Density of water (g/cm^3)

W_s = Weight of the pycnometer plus rock sample (g)

W_a = Weight of pycnometer filled with air (g)

W_{sw} = Weight of pycnometer filled with rock and air (g)

W_w = Weight of pycnometer filled with water (g)

Procedure for Liquid Pycnometry

Six different sample fractions in respective order, GRI+, size A, GRI, size B, size C including cubes (Table 3-2) were used for testing. Samples were first placed in a 60ºC oven for at least 48 hours and then placed in a desiccator for at least 30 minutes. Approximately 2 grams of fraction size sample were weighed. The pycnometers were then weighed in air, then again with the approximately 2 grams of sample (Figure 3-9). The pycnometer is then filled with fluid and a stopper is inserted carefully forcing excess fluid out of the capillary (Figure 3-10). A dry cloth is used to wipe any excess fluid outside the pycnometer. Afterward, the pycnometer including sample and desired fluid weight were measured. Weights are immediately measured within the first several seconds on the scale as a relative comparison of apparent bulk density results. Finally, the pycnometer and fluid weight were determined. DI water, THF, or DT2 fluids were used to displace weight and volume for this experiment with duplicate testing to receive more accurate results. The average and standard deviation of the duplicated results are calculated and plotted.

Figure 3-9: Pycnometer with approximately 2 grams of CLO-240 size C sample

Figure 3-10: Pycnometer filled with CLO-240 size C sample plus DI water

3-7 Mercury Intrusion Capillary Pressure (MICP)

MICP was performed on 8 dry 1cm^3 samples with an average weight of 2.5 grams with a Micrometritics Autopore IV 9520 system. MICP determines the porosity of the connected pores from the volume of injected mercury that intrudes the pore network under high pressures, and the capillary pressure curves from the volume of injected mercury under applied pressures at incremental increases. Pore-throat size distribution can be derived from the capillary pressure curves down to 3nm in diameter at a max of 60,000 psi (Rezaee, 2015). Mercury's characteristics consist of high surface energy and nonwetting tendencies to geological materials allowing only the external pressure to apply force into pores once capillary pressure is exceeded (Hu et al, 2015). The Washburn equation (Equation 3-3) exhibits that the intruded pore throat radius is

inversely proportional to the applied entry pressure (Washburn, 1921; Gao and Hu, 2013). The pore-throat radius can be determined by Laplace-Washburn equation (Washburn, 1921):

$$\Delta P = -\frac{2\gamma\cos\theta}{R} \quad \text{Equation 3-3}$$

OR

$$R = -\frac{2\sigma\cos\theta}{P_c} \quad \text{Equation 3-4}$$

Where:

ΔP = External pressure applied (Pa)

γ = Surface tension of mercury (485 dynes)

θ = Contact angle between mercury and pore wall (degree)

R = Pore throat radius (μm)

Constant surface tension and contact angle are assumed when utilizing the Washburn equation. It is noticed that the contact angle increases exponentially with decreasing pore diameters in unconventional reservoirs (Wang et al., 2016). The Washburn equation is therefore modified to apply a variable contact angle and surface tension (Equation 3-5). Equation 3-5 utilizes surface tension and contact angle as functions of the pore throat radius and assumes that all pores are cylindrical in shape. This is not an ideal scenario but gives a close approximation of pore size (Hu et al, 2015a). The function of R, f(R), is shown in Equation 3-6. The pore radius of f(R) = 0 corresponds to the pressure needed to overcome the pore's capillary pressure. The Newton-Raphson method is used as an algorithm to alternately solve the pore radius for a given pressure (Wang et al., 2016).

$$\Delta P = \frac{-2\gamma_{Hg}(R)\cos\theta_{Hg}(R)}{R}$$ Equation 3-5

$$(R) = p_c R + 2\gamma_{Hg}(R)\cos\theta_{Hg}(R)$$ Equation 3-6

Where:

p_c = Capillary pressure of intruded pore

Larger pore throats are invaded at low pressures while smaller pores are invaded at higher pressures. Mercury is injected at incremental pressure steps determining pore throat size distributions including porosity, permeability, bulk density, and tortuosity can be obtained. Pore size for this experiment ranges from 2.8 nm to 50 μm, dependent on penetrometers used which are related to sample porosities. MICP results can determine permeability by measuring pore throats at a maximum hydraulic conductance (Gao and Hu, 2013; Katz and Thompson, 1987) (Equation 3-7). Infection points are determined by the cumulative intrusion curves of pressure injected mercury into the sample. The pore-throat diameter will have a specific capillary pressure that is exceeded before mercury is intruded into the pore spaces. Each inflection point represents the intruded pore-throat diameter for a connected pore network.

$$k = \left(\frac{1}{89}\right)(L_{max})^2 \left(\frac{L_{max}}{L_c}\right)\phi S(L_{max})$$ Equation 3-7

Where:

k = Permeability (μ m^2)

L_{max} = Pore throat diameter at maximum hydraulic conductance when capillary pressure has been overcome by injected mercury of incremental pressures at specific pore diameters (μ m)

L_c = Pore throat diameter of intruded pore determined by inflection points on intrusion curves (μ m)

ϕ = Porosity (fractional)

S(L_{max}) = Mercury saturation at L_{max} (fractional)

Procedure for MICP

The 1cm^3 samples are first dried in a 60º C dry oven for at least 48 hours days prior to MICP testing. The MICP analysis was performed using the Micromeritics Autopore IV 9520 machine. After drying, the sample and penetrometer are weighed prior to testing. The sample is then placed in the penetrometer which is then inserted into the machine that is evacuated and in turn filled with mercury. Various penetrometers are used depending on variable porosity ranges that implement different filling pressures for the initial testing, allowing for analyses of variable pore sizes. For each experiment, two different analyses are performed first to apply low-pressures for detection of the larger μm size pores.

After low-pressure analysis was completed, the high-pressure analysis is performed from 30 psi up to 60,000 psi. The pressures are performed at increments starting from 5psi to 30psi and at each increment the pressure is equilibrated for 10 seconds prior to the next incremental pressure. Equilibration at high-pressure intrusion is set for 45 seconds. The mercury extrusion

curves are recorded as the pressure drops. The sample and penetrometer are then weighed after testing since mercury may still present and unable to fully extrude once the experiment is completed.

3-8 Spontaneous Imbibition and Vapor Absorption

Spontaneous Imbibition has been used as a reliable method to quantify the wettability of shales since a forced displacement in such low-permeable rocks requires a significant pressure drop, which may induce artificial cracks (Rezaee, 2015). Imbibition is the process in which capillary pressure drives and displaces a nonwetting fluid phase to a wetting fluid phase in a porous medium (Gao and Hu, 2012). In this study, air acts as the nonwetting fluid, DI water, and DT2 is utilized as the wetting fluid. The rate of imbibition is controlled by capillary pressure and permeability of the porous medium (Hu et al, 2001). Wettability of the fluid affects the changes in capillary pressure as the permeability is ultimately affected by the porosity and pore network. As fluid is imbibed onto a porous medium with respect to time, the cumulative imbibition vs. time graph can be expressed by Equation 3-8:

$$l(t)=St^{0.5} \qquad \text{Equation 3-8}$$

Where:

I(t) = Cumulative Imbibition (mm)

S = Sorptivity ($m/sec^{0.5}$)

t = Time (min)

The wetting surface of the imbibed fluid on a porous media are shown to have been affected by pore connectivity. The wetting front is affected by the edge accessible porosity

resulting in slower imbibition rates. If open fractures are present, the edge accessible porosity will equal to effective porosity causing the slope of the log cumulative vs. log time graph to equal 1. The imbibition slope in the well-connected pore systems are shown to have values close to 0.5 (Equation 3-8) as low connectivity will have vales close to 0.25 (Hu et al., 2012).

Vapor absorption procedures are similar to imbibition except for that the sample surface is suspended above a fluid rather having contact with it. The fluid imbibes the sample by the sample to fluid interface and/or vapor condensation by evaporation of fluid from petri dish (Hu et al., 2001). For imbibition experiments, buoyancy supports the sample when suspended in a fluid. As fluid is imbibed into the sample the fluid level decreases resulting in a decreased buoyancy force. As a result, the cumulative imbibition measurements become too heavy. Vapor absorption are compared with imbibition results without buoyancy force and vapor condensation affecting samples suspended above a fluid (Hu et al., 2001).

Procedure for Spontaneous imbibition and Vapor Absorption Experiments

The $1cm^3$ sample is dried in a 60º C oven for at least 48 hours prior to testing. The sample is then placed in a desiccator for about 30 minutes to cool to prevent the temperature change from affecting the sample weight. The initial fluid weights allotted in a petri dish were measured, DI water (water wetting fluid) and DT2 (oil wetting fluid). Two separate cubes were prepared for each sample test. One sample cube was used for Imbibition and Vapor Absorption tests using DI water and a separate cube was used for DT2 testing. Imbibition and vapor absorption testing using DI water was run prior to the DT2 testing. After each run, the sample

was returned to the oven for at least 48 hours to remove the imbibed water from previous experiment.

The Imbibition apparatus used to run the imbibition and vapor absorption experiments (Figure 3-11). The cubes and initial weights are measured using the Imbibition scale prior to testing. Once initial weights are recorded the cubes are hung from a custom-made holder with screws to keep the sample in place, the holder's opposite end has a hook to connect with the balance hanger. The chamber, placed beneath the balance, has a small 1-2mm hole to connect the hanger from the balance to the sample holder, to allow for suspension above the fluid. A petri dish containing the fluid is then carefully placed in the chamber. Once the sample is suspended directly above the fluid, the chamber is sealed and locked to maintain a constant relative humidity during the Imbibition and vapor absorption experiments. An adjustable jack beneath the chamber is used to allow the sample to raised or lowered to the desired height. A timer is set once the experiment starts and the weight measurements at predetermined time intervals are recorded by the Imbibition balance and transmitted to a connected computer.

For imbibition experiments, measurements are recorded at time intervals of every second for 2 minutes, then every 30 seconds until 1 hour has passed, then every 60 seconds until 6 hours have passed, and finally every 5 minutes for up to 24 hours. For vapor absorption experiments, measurements are taken every second for 30 seconds, every 2 minutes until 30 minutes have passed, every 5 minutes until 6 hours have passed, and finally every 10 minutes until 24 hours (for DT2) or 72 hours (for DI water) have passed. The DI water experiments were performed in duplicates to reduce errors in water surface tension effects by getting an average imbibition slope. The DI water imbibition tests were run on each sample for either 6, 12, or 24 hours. Vapor absorption for DI water was run for 72 hours. After the DI experiments were completed, DT2

was performed once for 8 hours for imbibition following a 48-hour experiment for vapor absorption.

Spot checks were periodically made to monitor the accuracy and recordings of each experiment. Once the imbibition test is complete, the sample is raised from the fluid by lowering the adjustable jack. The sample is immediately removed and quickly observed. Excess fluid is wiped off quickly by a premeasured moistened Kimwipe in the associated testing fluid (DI water or DT2). Once the sample is wiped the Kimwipe is weighed again to measure the amount of excess fluid. Immediately after, the sample and sample holder are then weighed. This measurement provides a reading against buoyancy effects and condensed fluid that may be present on the sample holder. Finally, the petri dish and the testing solution are weighed to monitor the cumulative imbibition measured by the computer and measure rate of evaporation. These experiments were used to determine pore connectivity, the measurements were then plotted by log cumulative imbibition and fluid saturation vs. log time.

Corrections were made for buoyancy and rate of evaporation based on the measurements made before and after testing completed. Once the experiment has initiated, there is often a time period of up to several seconds for the balance readings to stabilize and steadily increase. Slopes were determined and fit at different time intervals during the imbibition and/or absorption processes by graphical plotting the attained data.

Figure 3-11: Imbibition and vapor absorption setup with dish in the chamber and sample in suspension above the fluid.

Chapter 4 - Results

4-1 Vacuum Saturation

A compilation of vacuum saturation results (Table 4-1) conducted on all samples except for HNY outcrop. The HNY outcrop cube sample was too thin for vacuum saturation experiments, therefore is not included in the experiment. Three 1 cm cubes were tested with DI water, 1 cm cubes were tested with THF and DT2 fluids. This method is utilized to study the edge-only accessible porosity distribution of shale samples. Bulk density, sample porosity, and grain density average and standard deviation were calculated and used in conjunction with other methods discussed in this study. The bulk density calculated as it indicates the potential kerogen content of the rock due to its low grain density values.

Table 4-1: Summary of Vacuum Saturation Results

Sample ID	DI Water			THF			DT2		
	Bulk density (g/cm^3)	Grain density (g/cm^3)	**Porosity (%)**	Bulk density (g/cm^3)	Grain density (g/cm^3)	**Porosity (%)**	Bulk density (g/cm^3)	Grain density (g/cm^3)	**Porosity (%)**
EGSP-7378	2.476	2.679	7.593	2.543	2.776	8.384	2.470	2.671	7.518
EGSP-7418	2.405	2.911	17.366	2.462	2.992	17.700	2.363	2.889	18.213
EGSP-7461	2.307	2.732	15.528	3.132	3.671	14.686	2.442	2.889	15.469
EGSP-7495	2.584	2.824	8.488	2.716	2.962	8.279	2.378	2.606	8.763
EGSP-4020	2.372	2.819	15.849	2.474	2.938	15.790	2.455	2.938	16.449
EGSP-4036	2.300	2.862	19.632	2.393	2.924	18.168	2.422	2.941	17.633
EGSP-4081	2.129	2.592	17.858	2.419	2.940	17.731	2.455	2.947	16.713
EGSP-4122	2.253	2.432	7.366	2.296	2.465	6.874	2.424	2.623	7.608
BE-248	2.557	2.869	10.870	2.556	2.847	10.232	2.371	2.648	10.490
BE-289	2.464	2.551	3.411	2.626	2.734	3.933	2.390	2.474	3.396
BE-342	2.458	2.568	4.283	2.571	1.154	4.731	2.528	2.635	4.030
BNT-8299	2.330	2.635	11.559	1.991	2.259	11.857	2.496	2.828	11.744
BNT-8300	2.379	2.716	12.410	2.344	2.704	13.316	2.460	2.811	12.477
BNT-8327	2.225	2.515	11.526	1.927	2.164	10.934	2.112	2.379	11.198
BEC Outcrop	2.364	2.611	9.469	2.467	2.724	9.424	2.479	2.731	9.218
HNY Outcrop	-	-	-	-	-	-	-	-	-
CLO-240	2.505	2.767	9.490	2.506	2.799	10.490	2.613	2.885	9.427

4-2 Wettability and Contact Angle

As previously discussed, the wettability of the surface of a sample is quantified by measuring the contact angle of a droplet of the wetting liquid with respect to time. Raw data images of this process are displayed in Figure 4-1, and an example of the results are shown in Table 4-2. Measurements were taken at incremental time intervals (Figure 4-2) for each fluid until the contact angle becomes unvarying. Contact angle values are shown at 30 seconds for DI water, API brine, and 10% THF. Whereas the highly volatile DT2 values are instantly measured due to the instrument's 3-degree detection limit in less than one second. The results of contact angle measurements show that samples are water-wet but show characteristics of absorption of THF and DT2 except for EGSP-4122 which is not wetting to water (Figure 4-1).

A)

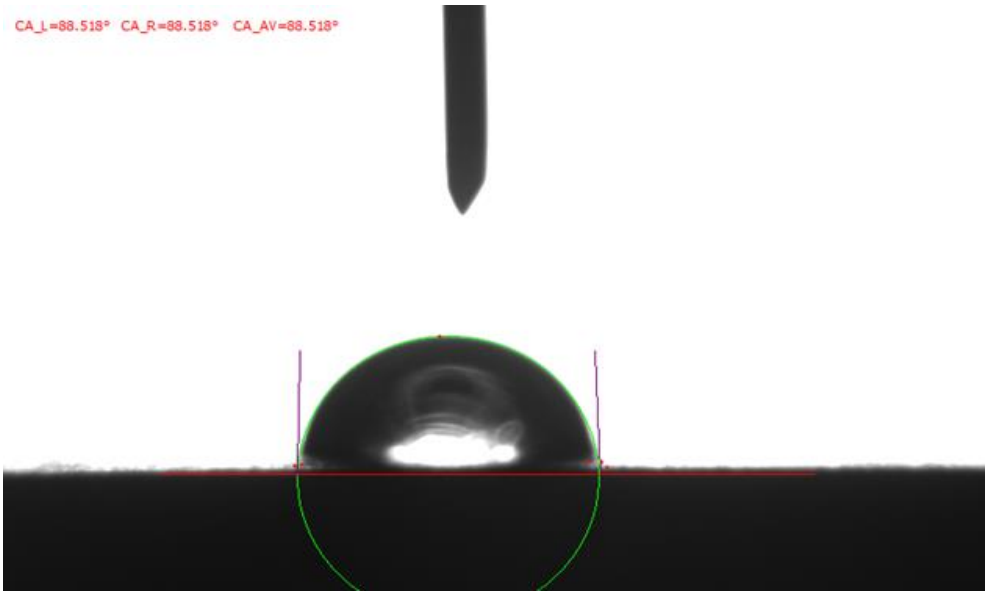

B)

Figure 4-1: Images of DI water droplets A) before and B) after surface contact angle measurements for sample EGSP-4122.

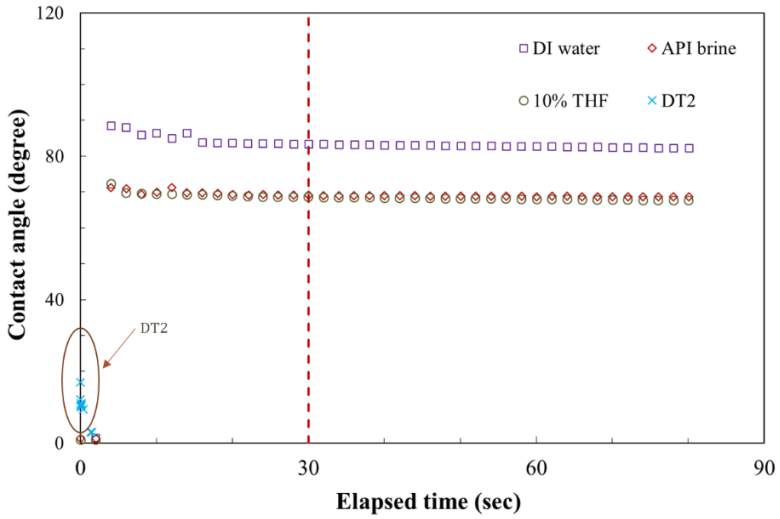

Figure 4-2: Contact angle vs. time graph for different fluids on EGSP-4122 sample surface.

Table 4-2: Contact angle summary for each fluid type.

Sample ID	DI water	API brine	10% THF	DT2
EGSP-7378	24.160	16.574	11.998	12.084
EGSP-7418	15.766	14.992	15.673	12.985
EGSP-7461	28.061	20.585	17.883	13.438
EGSP-7495	18.247	23.477	28.098	14.450
EGSP-4020	11.798	17.945	12.368	12.481
EGSP-4036	18.690	24.309	2.875	14.788
EGSP-4081	22.875	9.143	15.493	18.740
EGSP-4122	83.332	69.077	68.574	17.006
BE-248	23.288	39.214	35.851	15.629
BE-289	52.702	34.831	1.432	13.972
BE-342	35.860	23.311	35.068	13.279
BNT-8299	26.725	14.027	7.931	13.276
BNT-8300	7.182	16.519	6.003	12.211
BNT-8327	20.077	16.404	3.422	11.774
BEC Outcrop	37.932	49.469	43.258	16.604
HNY Outcrop	12.180	11.976	7.970	13.506
CLO-240	18.051	24.613	11.969	10.578

Note: Contact angle values are shown at 30 sec for DI water, API brine, and 10% THF, while DT2 drops below detection limit of <3 degrees in less than a second.

4-3 Mineralogy

The mineral composition of the samples typically consists of higher percentages of quartz and feldspar with an outlying carbonate sample (Figure 4-3). This may be due to the interbedded limestone and carbonate layers within the Marcellus. Based on the lithofacies diagram, most Marcellus samples are clay-rich siliceous mudstones to siliceous mudstones. Some Marcellus samples are mixed to silica-dominated lithotype. The Utica sample consist of a silica-rich carbonate mudstone. Mineralogical percentages of each sample are shown in Table 4-4.

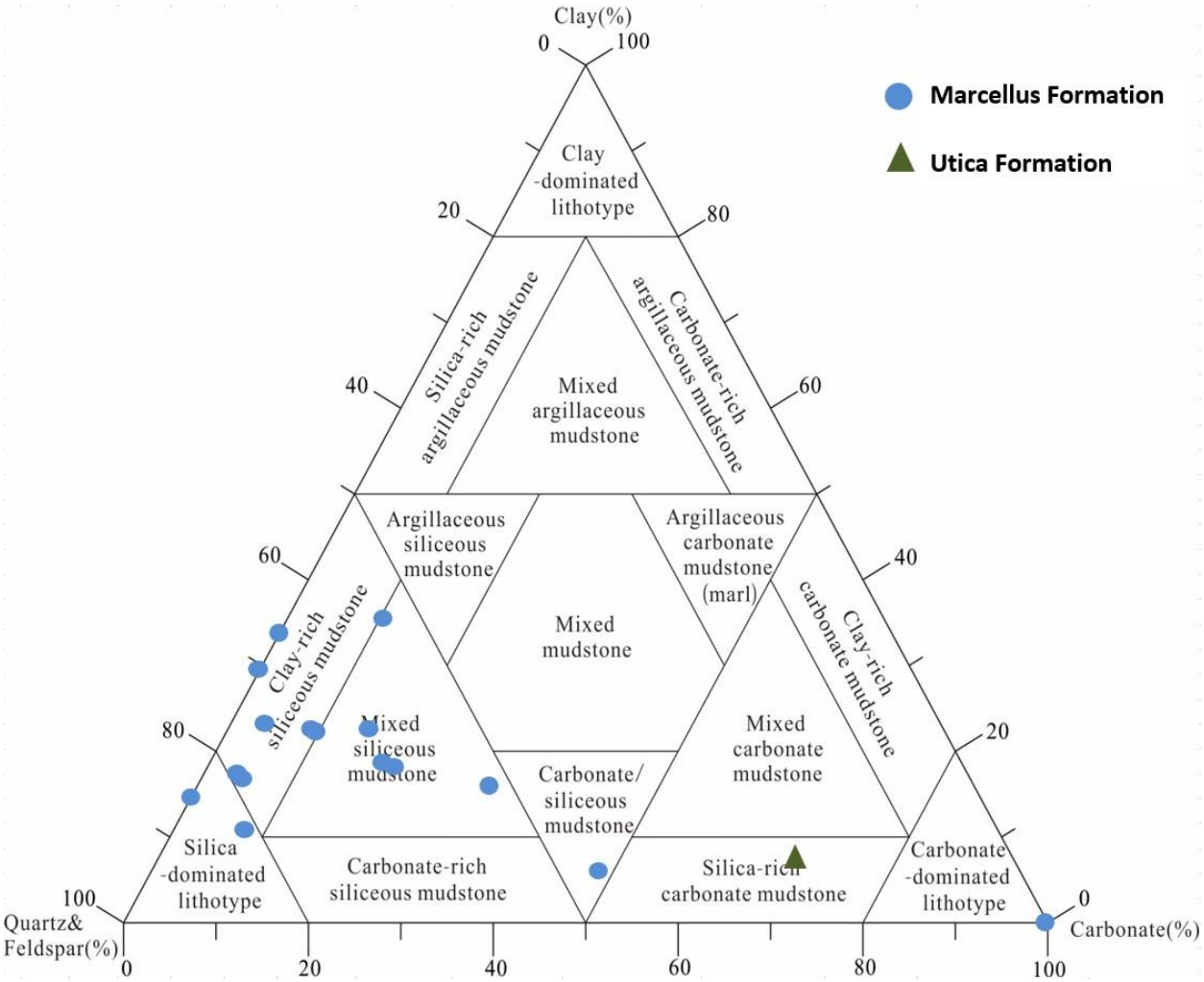

Figure 4-3: Schlumberger (2014) ternary lithofacies diagram with plotted samples.

Table 4-3: Mineralogical weight percentages of study samples

Sample ID	Quartz	Pyrite	Albite	Anorthite	Calcite	Ankerite	Dolomite	Kutnohorite	Brushite	Baryte	Ulvospinel	Fraipontite	Illite	Clinochlore	Montmorillonite	Halloysite	Phengite	Mica
	Silica	Sulfide	Feldspar		Carbonate				Phosphate	Sulfate	Oxide	Hydroxide	Clay					
	(Weight %)																	
EGSP-7378	50.2 ± 2.9	3.6 ± 0.3	3.4 ± 0.3	7.9 ± 0.5							4.8 ± 0.5	0.5 ± 0.2	3.2 ± 0.4	2.7 ± 0.2	7 ± 0.6			16.6 ± 1.1
EGSP-7418	37.2 ± 2.2	4.2 ± 0.3	16.4 ± 1.2								8.4 ± 0.7		15.7 ± 1	2.1 ± 0.2	4.6 ± 0.4			11.4 ± 0.9
EGSP-7461	43.5 ± 2.5	6.7 ± 0.4	2.1 ± 0.3	4 ± 0.4	20.4 ± 1.2						5 ± 0.5		7.6 ± 0.6		2 ± 0.3			8.7 ± 0.7
EGSP-7495	0.5 ± 0.1				99.5 ± 7.1													
EGSP-4020	28.7 ± 1.6	5.2 ± 0.4	5.8 ± 0.5		25.2 ± 1.9	6.6 ± 0.5					6.1 ± 0.6	6.2 ± 0.5	10.3 ± 0.7	1.6 ± 0.1	4 ± 0.4			
EGSP-4036	37 ± 2.1			7.1 ± 0.5	6.2 ± 0.5		9.1 ± 0.8		3.8 ± 0.4		6.8 ± 0.5	7.5 ± 0.7	11.8 ± 0.8	6.8 ± 0.5	4.1 ± 0.4			
EGSP-4081	33.4 ± 1.9	1.9 ± 0.2	4.7 ± 0.5	5.3 ± 0.5	10.5 ± 0.7						2.9 ± 0.5	5.9 ± 0.6		7.3 ± 0.5	5.5 ± 0.5			22.7 ± 1.2
EGSP-4122	19 ± 1.4	17.2 ± 1.3	2.7 ± 0.5		46.3 ± 5.9	1.3 ± 0.2	0.9 ± 0.2				6.6 ± 0.6				3 ± 0.4			2.9 ± 0.3
BE-248	32.9 ± 1.9	6.6 ± 0.4	1.9 ± 0.5	4.9 ± 0.4	3.6 ± 0.5			5.5 ± 0.6		5.5 ± 0.3	9.5 ± 0.7	6.9 ± 0.5	9.9 ± 0.7	1.3 ± 0.2	4.4 ± 0.4	7 ± 0.8		
BE-289	40.3 ± 2.3	8.4 ± 0.5	1 ± 0.2	4.9 ± 0.4				3.6 ± 0.4		5.6 ± 0.4	11 ± 0.8	7.9 ± 0.6	10 ± 0.7	1.1 ± 0.1	6.3 ± 0.5			
BE-342	34.2 ± 2	9.4 ± 0.6	5.7 ± 0.5	8.5 ± 0.6	3.8 ± 0.4					6.8 ± 0.4	8.3 ± 0.7		13 ± 0.9	2.5 ± 0.2	3.2 ± 0.4	4.5 ± 0.7		
BNT-8299	44.9 ± 2.6	6.5 ± 0.5	9.7 ± 0.7		9.7 ± 0.7							6.8 ± 0.5	12.3 ± 0.8	2.5 ± 0.2	1.8 ± 0.3	2.7 ± 0.3	3.1 ± 0.3	
BNT-8300	37.7 ± 2.2	5.6 ± 0.4	10.1 ± 0.7		18.8 ± 1.1						6 ± 0.7	3.2 ± 0.3	10.7 ± 0.8	2.8 ± 0.2	0.5 ± 0.2	3.4 ± 0.3	1.2 ± 0.3	
BNT-8327	56.8 ± 3.4	7.5 ± 0.5	13.2 ± 0.8		7.8 ± 0.6						3.9 ± 0.4		6.8 ± 0.6			4.1 ± 0.3		
BE-Creek Outcrop	64.1 ± 3.9	10.2 ± 0.7			4.6 ± 0.5						4.2 ± 0.6		5 ± 0.5	1.9 ± 0.2			1.7 ± 0.3	8.2 ± 0.6
HNY Outcrop	59.9 ± 3.6			8.9 ± 0.6							16.6 ± 1.2		9.1 ± 0.7					5.5 ± 0.4
CLO-240	22 ± 1.3	1.3 ± 0.1		0.7 ± 0.1	60.9 ± 3.7		7.8 ± 0.5				0.1 ± 0		1.8 ± 0.2					5.5 ± 0.4

4-4 Geochemistry

Geochemical data from all samples discussed in this study are shown in Table 4-4. TOC ranges from 0.51 to 12.3%, S1 values range from 0.06 to 4.69 mg HC/g with HNY-Outcrop having 0.03 mg HC/g. Vitrinite reflectance is determined from T_{max} values, this enables a kerogen conversion (PI) verses T_{max} to be plotted in Figure 4-4. According to the Pseudo van Krevelen plot (Figure 4-5), kerogen maturation is from a combination of Type II and Type III for majority of the samples. Since majority of the sample data plotted in the lower left corner of the graph. The Bald Eagle well including, EGSP-4020, EGSP-4122, BEC-outcrop, and CLO-240 have %Ro that fall into the mature to overmature catagenesis phases. From the kerogen quality plot in (Figure 4-6), samples are type III gas prone to dry gas prone.

Table 4-4: Geochemical analysis for all samples discussed in this study.

Sample ID	TOC (wt%)	S1 (mg HC/g)	S2 (mg HC/g)	S3 (mg CO2/g)	T_{MAX} (°C)	Calculated %Ro (From T_{MAX})	Hydrogen Index (S2x100/TOC)	Oxygen Index (S3x100/TOC)	Production Index (S1/(S1+S2)
EGSP-7378	2.42	0.09	0.10	0.26	425	0.49	4	11	0.47
EGSP-7418	3.63	0.14	0.05	0.36	320	0	1	10	0.74
EGSP-7461	4.95	0.21	0.23	0.27	320	0	5	5	0.48
EGSP-7495	0.51	0.06	0.18	0.36	419	0.38	36	71	0.25
EGSP-4020	0.78	0.40	0.70	0.33	451	0.96	89	42	0.36
EGSP-4036	0.95	0.62	0.86	0.26	456	1.05	91	27	0.42
EGSP-4081	1.03	0.69	0.97	0.33	456	1.05	94	32	0.42
EGSP-4122	12.30	4.69	20.27	0.36	441	0.78	165	3	0.19
BE-248	2.67	0.62	1.10	0.32	465	1.21	41	12	0.36
BE-289	2.39	0.40	0.95	0.22	461	1.14	40	9	0.30
BE-342	3.27	0.62	1.68	0.24	467	1.25	51	7	0.27
BNT-8299	3.89	0.54	0.27	0.22	316	0	7	6	0.67
BNT-8300	6.55	0.95	0.53	0.37	322	0	8	6	0.64
BNT-8327	8.70	0.54	0.22	0.36	311	0	3	4	0.71
BEC-Outcrop	4.85	0.34	2.60	0.28	475	1.39	54	6	0.12
HNY-Outcrop	3.45	0.03	0.09	0.48	424	0.47	3	14	0.25
CLO-240	2.96	0.07	0.25	0.18	439	0.74	8	6	0.22

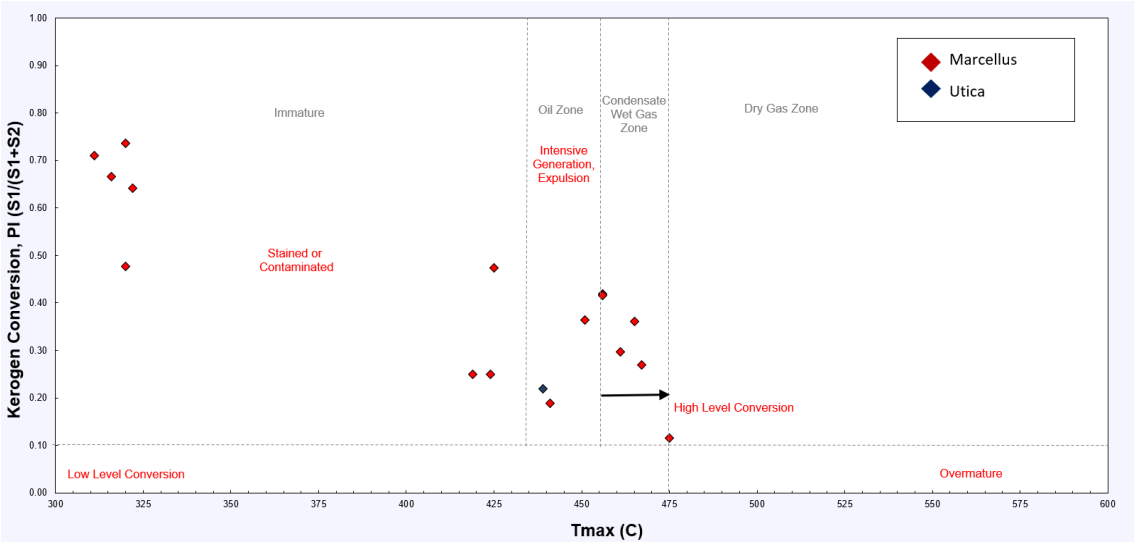

Figure 4-4: Kerogen quality plot of PI vs. T_{max}.

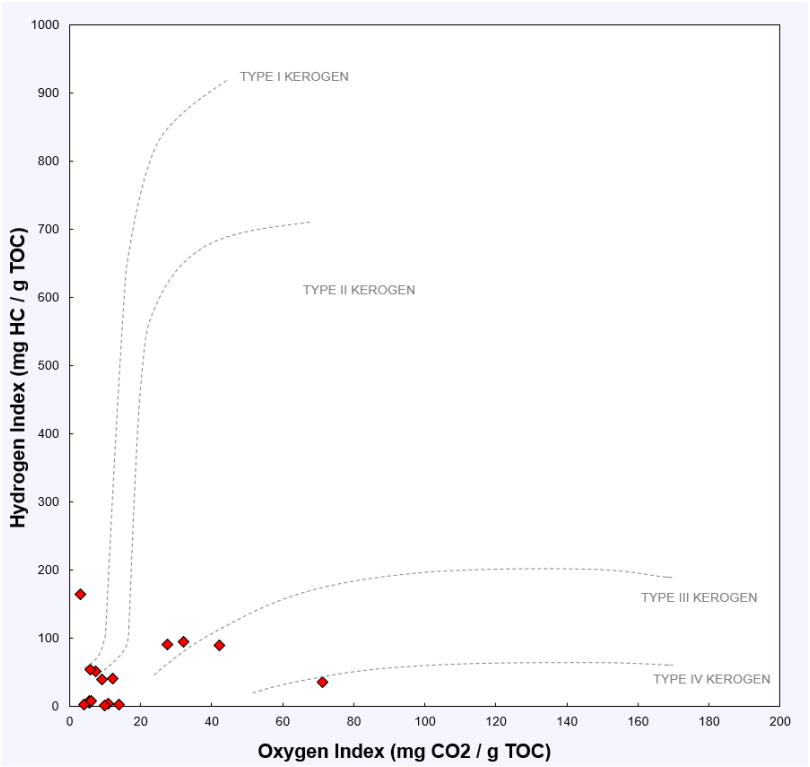

Figure 4-5: Pseudo van Krevelen plot of HI vs. OI to determine kerogen type and maturity.

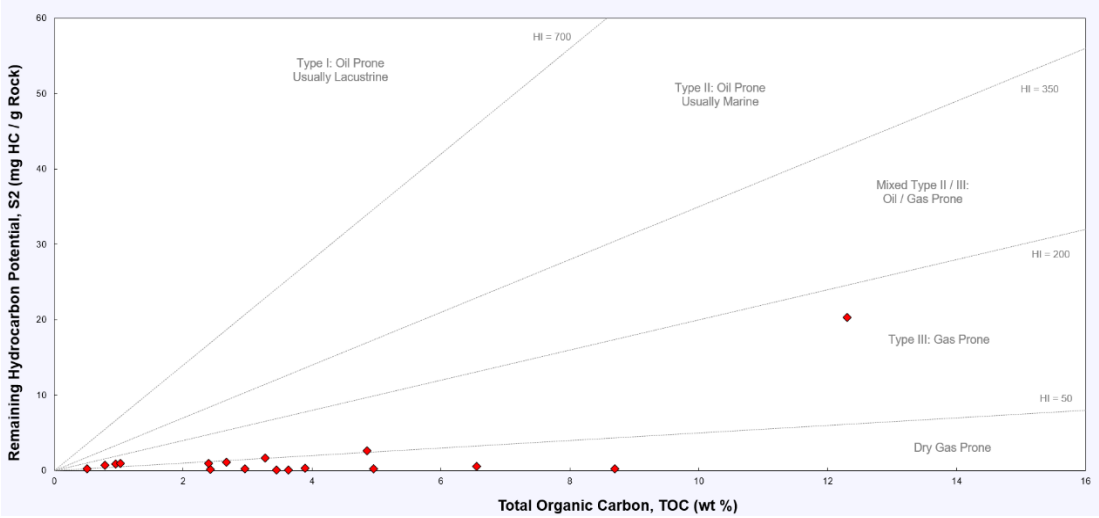

Figure 4-6: Kerogen quality plot determined by S2 vs. TOC%.

4-5 Liquid Pycnometry

Liquid displacement was used by the pycnometer method to calculate bulk density which is the density of solid particles in a volume. As previously discussed, particle density can be calculated from porosity and bulk density by carefully measuring mass and volume. For comparison, sample size fractions are converted to their equivalent spherical diameters in μm (Table 4-5), and bulk density is calculated by fluid displacement of DI water, THF, and DT2.

Table 4-5: Calculated bulk density by fluid displacement of DI water, THF, and DT2 for each sample.

Sample ID	Size designation	Size	Equivalent spherical diameter (µm)	DI Water (g/cm^3)	THF (g/cm^3)	DT2 (g/cm^3)
EGSP-7378	Cube	Cube (1 cm side)	6204	2.538±0.015	2.551±0.02	2.563±0.009
	GRI+	1.70 - 2.36 mm	2030			
	Size A	841 - 1700 µm	1271			
	GRI	500 - 841 µm	671			
	Size B	177 - 500 µm	339	2.541±0.004	2.518±0.02	2.522±0.01
	Size C	75 - 177 µm	126	2.534±0.007	2.515±0.002	2.527±0.01
EGSP-7418	Cube	Cube (1 cm side)	6204	2.5296±0.004	2.495±0.021	2.499±0.004
	GRI+	1.70 - 2.36 mm	2030	2.513±0.016	2.529±0.025	2.489±0.01
	Size A	841 - 1700 µm	1271			
	GRI	500 - 841 µm	671	2.509±0.009	2.506±0.016	2.471±0.025
	Size B	177 - 500 µm	339	2.482±0.002	2.477±0.01	2.473±0.025
	Size C	75 - 177 µm	126	2.487±0	2.485±0.011	2.494±0.019
EGSP-7461	Cube	Cube (1 cm side)	6204	2.476±0.014	2.452±0.024	2.460±0.003
	GRI+	1.70 - 2.36 mm	2030	2.479±0.006	2.472±0.011	2.468±0.01
	Size A	841 - 1700 µm	1271			
	GRI	500 - 841 µm	671	2.477±0.006	2.476±0.01	2.482±0.011
	Size B	177 - 500 µm	339	2.474±0.001	2.475±0.01	2.465±0.009
	Size C	75 - 177 µm	126	2.475±0.002	2.477±0.011	2.462±0.01
EGSP-7495	Cube	Cube (1 cm side)	6204	2.711±0.012	2.715±0.017	2.685±0.02
	GRI+	1.70 - 2.36 mm	2030	2.735±0.002	2.724±0.012	2.705±0.011
	Size A	841 - 1700 µm	1271			
	GRI	500 - 841 µm	671	2.733±0.002	2.717±0.013	2.717±0.009
	Size B	177 - 500 µm	339	2.719±0.003	2.713±0.012	2.721±0.013
	Size C	75 - 177 µm	126	2.705±0.006	2.718±0.014	2.728±0.015
EGSP-4020	Cube	Cube (1 cm side)	6204	2.548±0.006	2.531±0.006	2.532±0.006
	GRI+	1.70 - 2.36 mm	2030	2.547±0.005	2.564±0.011	2.567±0.012
	Size A	841 - 1700 µm	1271			
	GRI	500 - 841 µm	671	2.537±0.002	2.555±0.012	2.547±0.01
	Size B	177 - 500 µm	339	2.525±0.005	2.512±0.01	2.51±0.009
	Size C	75 - 177 µm	126	2.527±0.002	2.516±0.011	2.521±0.012

Table 4-5 Continued:

Sample ID	Size designation	Size	Equivalent spherical diameter (µm)	DI Water (g/cm^3)	THF (g/cm^3)	DT2 (g/cm^3)
EGSP-4036	Cube	Cube (1 cm side)	6204	2.542±0.001	2.547±0.01	2.544±0.005
	GRI+	1.70 - 2.36 mm	2030	2.569±0.003	2.563±0.006	2.554±0.009
	Size A	841 - 1700 µm	1271			
	GRI	500 - 841 µm	671	2.567±0.005	2.579±0.011	2.564±0.008
	Size B	177 - 500 µm	339	2.562±0.004	2.576±0.006	2.567±0.01
	Size C	75 - 177 µm	126	2.574±0.004	2.566±0.006	2.572±0.008
EGSP-4081	Cube	Cube (1 cm side)	6204	2.595±0.02	2.612±0.013	2.576±0.017
	GRI+	1.70 - 2.36 mm	2030			
	Size A	841 - 1700 µm	1271			
	GRI	500 - 841 µm	671	2.582±0.006	2.571±0.005	2.577±0.015
	Size B	177 - 500 µm	339	2.582±0.002	2.584±0.01	2.571±0.008
	Size C	75 - 177 µm	126	2.585±0.001	2.59±0.011	2.564±0.011
EGSP-4122	Cube	Cube (1 cm side)	6204	2.323±0.027	2.299±0.011	2.340±0.009
	GRI+	1.70 - 2.36 mm	2030			
	Size A	841 - 1700 µm	1271			
	GRI	500 - 841 µm	671	2.353±0.007	2.348±0.009	2.349±0.007
	Size B	177 - 500 µm	339	2.326±0.002	2.331±0.007	2.329±0.008
	Size C	75 - 177 µm	126	2.328±0.002	2.327±0.017	2.321±0.009
BE-248	Cube	Cube (1 cm side)	6204	2.716±0.018	2.702±0.015	2.730±0.009
	GRI+	1.70 - 2.36 mm	2030	2.673±0.008	2.682±0.009	2.672±0.009
	Size A	841 - 1700 µm	1271			
	GRI	500 - 841 µm	671	2.668±0.007	2.683±0.009	2.677±0.009
	Size B	177 - 500 µm	339	2.676±0.006	2.682±0.009	2.667±0.011
	Size C	75 - 177 µm	126	2.668±0.006	2.684±0.01	2.667±0.012
BE-289	Cube	Cube (1 cm side)	6204	2.661±0.007	2.673±0.005	2.686±0.011
	GRI+	1.70 - 2.36 mm	2030	2.661±0.013	2.678±0.014	2.675±0.011
	Size A	841 - 1700 µm	1271			
	GRI	500 - 841 µm	671	2.675±0.009	2.679±0.007	2.672±0.011
	Size B	177 - 500 µm	339	2.675±0.004	2.675±0.008	2.682±0.012
	Size C	75 - 177 µm	126	2.67±0.001	2.679±0.01	2.678±0.009

Table 4-5 Continued:

Sample ID	Size designation	Size	Equivalent spherical diameter (µm)	DI Water (g/cm^3)	THF (g/cm^3)	DT2 (g/cm^3)
BE-342	Cube	Cube (1 cm side)	6204	2.640±0.003	2.620±0.017	2.634±0.015
	GRI+	1.70 - 2.36 mm	2030	2.636±0.004	2.642±0.007	2.63±0.012
	Size A	841 - 1700 µm	1271			
	GRI	500 - 841 µm	671	2.636±0.004	2.61±0.027	2.633±0.008
	Size B	177 - 500 µm	339	2.622±0.004	2.597±0.006	2.604±0.007
	Size C	75 - 177 µm	126	2.617±0.006	2.614±0.009	2.616±0.012
BNT-8299	Cube	Cube (1 cm side)	6204	2.583±0.015	2.550±0.015	2.563±0.019
	GRI+	1.70 - 2.36 mm	2030	2.555±0.005	2.565±0.009	2.572±0.016
	Size A	841 - 1700 µm	1271			
	GRI	500 - 841 µm	671	2.553±0.002	2.576±0.004	2.559±0.011
	Size B	177 - 500 µm	339	2.546±0.008	2.568±0.006	2.56±0.01
	Size C	75 - 177 µm	126	2.563±0	2.562±0.004	2.553±0.004
BNT-8300	Cube	Cube (1 cm side)	6204	2.441±0.014	2.455±0.007	2.456±0.005
	GRI+	1.70 - 2.36 mm	2030	2.471±0.003	2.465±0.006	2.462±0.001
	Size A	841 - 1700 µm	1271			
	GRI	500 - 841 µm	671	2.451±0.003	2.467±0.009	2.442±0.004
	Size B	177 - 500 µm	339	2.446±0.003	2.456±0.001	2.444±0.009
	Size C	75 - 177 µm	126	2.43±0.004	2.416±0.003	2.422±0.016
BNT-8327	Cube	Cube (1 cm side)	6204	2.392±0.006	2.363±0.013	2.361±0.010
	GRI+	1.70 - 2.36 mm	2030	2.39±0.002	2.383±0.003	2.397±0.008
	Size A	841 - 1700 µm	1271			
	GRI	500 - 841 µm	671	2.4±0.005	2.392±0.003	2.379±0.012
	Size B	177 - 500 µm	339	2.382±0.002	2.382±0.002	2.388±0.006
	Size C	75 - 177 µm	126	2.379±0.006	2.394±0.009	2.376±0.007
BEC-OUTCROP	Cube	Cube (1 cm side)	6204	2.489±0.023	2.461±0.01	2.468±0.006
	GRI+	1.70 - 2.36 mm	2030	2.478±0.005	2.463±0.007	2.481±0.012
	Size A	841 - 1700 µm	1271			
	GRI	500 - 841 µm	671	2.461±0.005	2.449±0.011	2.451±0.005
	Size B	177 - 500 µm	339	2.462±0.005	2.463±0.006	2.449±0.005
	Size C	75 - 177 µm	126	2.447±0.006	2.441±0.007	2.437±0.005

Table 4-5 Continued:

Sample ID	Size designation	Size	Equivalent spherical diameter (μm)	DI Water (g/cm^3)	THF (g/cm^3)	DT2 (g/cm^3)
HNY-OUTCROP	Cube	Cube (1 cm side)	6204	2.321±0.003	2.336±0.023	2.339±0.022
	GRI+	1.70 - 2.36 mm	2030	2.31±0.006	2.311±0.005	2.306±0.009
	Size A	841 - 1700 μm	1271			
	GRI	500 - 841 μm	671	2.310±0.012	2.294±0.006	2.301±0.012
	Size B	177 - 500 μm	339	2.295±0.002	2.286±0.008	2.284±0.008
	Size C	75 - 177 μm	126	2.287±0.004	2.269±0.005	2.268±0.004
CLO-240	Cube	Cube (1 cm side)	6204	2.603±0.002	2.589±0.013	2.612±0.008
	GRI+	1.70 - 2.36 mm	2030			
	Size A	841 - 1700 μm	1271			
	GRI	500 - 841 μm	671	2.579±0.008	2.574±0.007	2.585±0.007
	Size B	177 - 500 μm	339	2.575±0.002	2.573±0.007	2.570±0.003
	Size C	75 - 177 μm	126	2.576±0.008	2.567±0.010	2.559±0.007

4-6 Mercury Intrusion Capillary Pressure (MICP)

MICP method is used to determine pore throat distribution in porous media by mercury invasion at variable pore pressures. Other quantifiable petrophysical properties include permeability, tortuosity, pore volume, density can be calculated utilizing such method. EGSP-7461, EGSP-7495, EGSP-4036, EGSP-4081, EGSP-4122, BNT-8299, BNT-8327, and CLO-240 were tested with MICP. MICP inflection points (IPs) are determined by peaks in intrusion pressures (Figure 4-7). Pore types are dependent on variable pore throat diameters: 50-1 μm size range are related to existing micro-fractures in the rock. 0.5-1 μm size defines the interparticle pore space. 50-10 nm sizes define the intraparticle pore spaces. 10-5 nanometers (nm) pores are organic pores caused by

conversion of organic matter into hydrocarbons. 5-2.8 nm pore sizes are accessible spaces between clay grains that have been intruded.

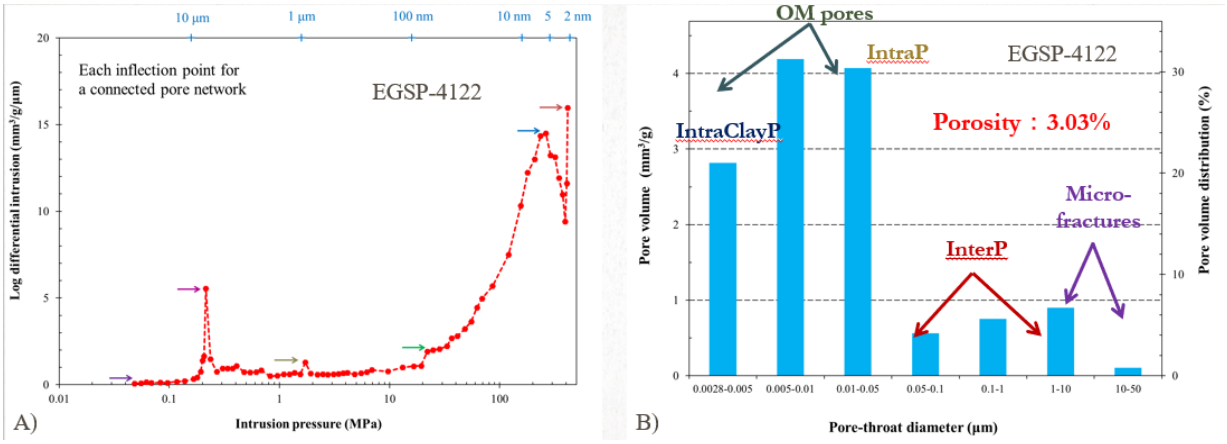

Figure 4-7: A) EGSP-4122 sample displaying IPs at variable intrusion pressures. B) Displaying pore-throat distribution percentages.

Majority of the samples have 10-50 µm pore-throat diameters with relatively high interparticle to intraparticle pore-throat distributions (Figure 4-8) (Table 4-6). EGSP-7461, EGSP-4036, and EGSP-4122 have higher 2.8-5 nm pore-throat sizes. Organic ores <12.3 nm (Pommer and Milliken, 2015) are existent in all samples except for EGSP-7495 and CLO-240. Samples EGSP-7461 (5.18%), EGSP-7495 (1.3%), had low porosities with extremely low porosity for CLO-240 (0.17%). Original porosity ranges from 1.3% to 30.31% for the Marcellus samples and 0.17% for the Utica sample. Additional quantifiable petrophysical characteristics are shown in Table 4-7.

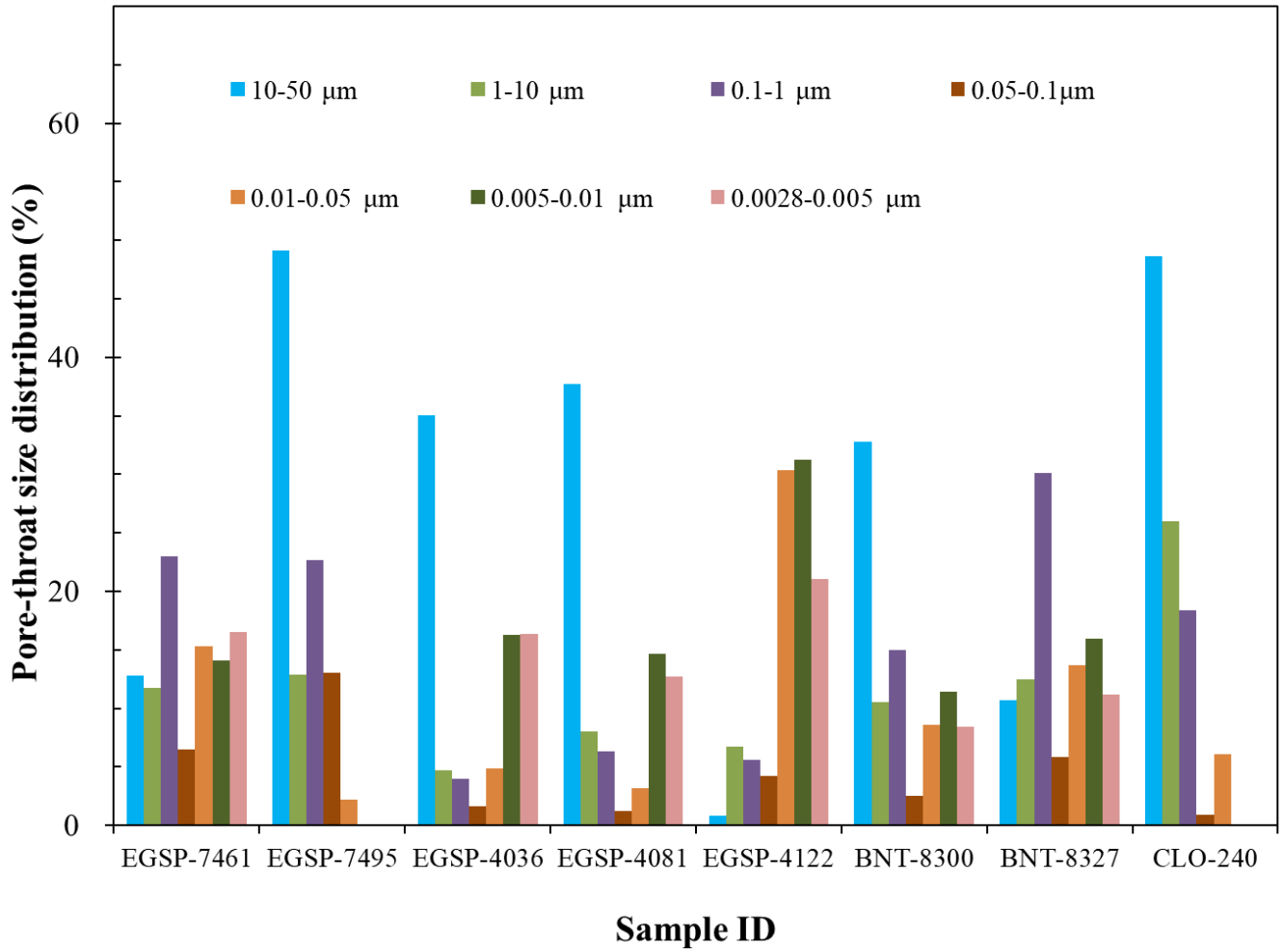

Figure 4-8: Histograms of pore-throat size distribution.

Table 4-6: Cumulative pore-throat size diameters (%)

Sample ID	Pore-throat diameter %						
	(10-50 µm)	**(1-10 µm)**	**(0.1-1 µm)**	**(0.05-0.1 µm)**	**(0.01-0.05 µm)**	**(0.005-0.01 µm)**	**(0.0028-0.005 µm)**
EGSP-7461	12.76	11.7	22.97	6.52	15.34	14.13	16.56
EGSP-7495	49.13	12.9	22.68	13.08	2.24		
EGSP-4036	35.05	4.71	3.98	1.65	4.86	16.27	16.38
EGSP-4081	37.68	8.03	6.35	1.25	3.17	14.7	12.74
EGSP-4122	0.79	6.72	5.62	4.21	30.37	31.28	21.02
BNT-8300	32.8	10.5	15.0	2.56	8.6	11.46	8.4
BNT-8327	10.73	12.47	30.09	5.85	13.73	15.93	11.21
CLO-240	48.7	26.0	18.36	0.9	6.1		

Table 4-7: Compilation of MICP results with respect to multiple μm-nm pore networks

Sample ID	Pore-throat region	Total intrusion volume (cm^3/g)	Total pore area (m^2/g)	Median pore-throat diameter D_{50} (Volume) (μm)	Bulk density (g/cm^3)	Porosity (%)	Pore volume (%)	Permeability (mD)	Tortuosity (D0/De)
EGEP-7461	10-50 um	0.2	3.06	59.14	2.4	5.18	0.13	9.751E+00	2.83
	1-10 um						0.12	6.147E-01	11.26
	0.1-1 um						0.23	1.500E-03	228.02
	10-100 nm						0	0	0
	5-10 nm						0.14	4.171E-06	4324.17
	2.8-5 nm						0.17	4.494E-06	4165.52
EGSP-7495	10-50 um	0.00	0.09	6864.84	2.63	1.3	0.49	1.327E+00	11.05
	1-10 um						0.13	3.124E-01	22.8
	0.1-1 um						0.23	1.261E-02	113.33
	10-100 nm						0.15	1.787E-04	951.85
	5-10 nm						0	0	0
	2.8-5 nm						0	0	0
EGSP-4036	10-50 um	0.04	12.6	10479.01	2.37	9.31	0	0	0
	1-10 um						0.05	3.073E+02	11.73
	0.1-1 um						0.04	1.599E+00	162.64
	10-100 nm						0.07	7.730E-03	2339.12
	10-50 nm						0.16	1.792E-05	48584.32
	5-10 nm						0.08	1.264E-05	57841.08
	2.8-5 nm						0.08	1.264E-05	57841.08
EGSP-4081	10-50 um	0.05	14.1	11132.34	2.27	12.1	0	0	0
	1-10 um						0.08	1.354E+03	7.73
	0.1-1 um						0.06	7.679E+01	32.45
	10-100 nm						0.04	2.801E-02	1698.81
	10-50 nm						0.15	3.727E-04	14727.4
	5-10 nm						0.06	2.589E-05	55871.89
	2.8-5 nm						0.06	1.528E-05	72745.72

Table 4-7 Continued:

Sample ID	Pore-throat region	Total intrusion volume (cm^3/g)	Total pore area (m^2/g)	Median pore-throat diameter D_{50} (Volume) (µm)	Bulk density (g/cm^3)	Porosity (%)	Pore volume (%)	Permeability (mD)	Tortuosity (D0/De)
EGSP-4122	10-50 um	0.01	7.39	7.6	2.26	3.03	0.01	2.672E-01	4.16
	1-10 um						0.07	9.155E-03	22.48
	0.1-1 um						0.06	8.400E-04	74.21
	10-100 nm						0.35	9.727E-05	218.06
	5-10 nm						0.31	3.098E-06	1221.97
	2.8-5 nm						0.21	2.720E-06	1304.09
BNT-8300	10-50 um	0.05	10.29	1541.71	2.27	11.47	0	0	0
	1-10 um						0	0	0
	0.1-1 um						0.11	8.058E-01	208.04
	10-100 nm						0.18	5.778E-03	2456.94
	10-50 nm						0.09	1.005E-05	58906.87
	5-10 nm						0.06	1.318E-05	51441.09
	2.8-5 nm						0.06	1.318E-05	51441.09
BNT-8327	10-50 um	0.04	12.01	101.01	2.26	9.41	0.11	1.635E+01	2.84
	1-10 um						0.12	8.299E-01	12.6
	0.1-1 um						0.30	1.635E+01	2.84
	10-100 nm						0.20	3.038E-03	208.25
	5-10 nm						0.16	1.808E-05	2699.36
	2.8-5 nm						0.11	6.992E-06	4340.51
CLO-240	10-50 um	0.0	0.01	7101.97	2.57	0.17	0.49	1.730E+00	3.3
	1-10 um						0.26	5.250E-02	18.93
	0.1-1 um						0.18	1.118E-02	41.03
	10-100 nm						0.07	2.020E-05	965.34
	5-10 nm						0	0	0
	2.8-5 nm						0	0	0

4-7 Fluid Imbibition and Vapor Absorption

DI and DT2 fluids were used to for imbibition and vapor absorption experiments. Imbibition experiments were run with duplicates of 6, 12, or 24-hour time span to reduce error with surface tension. Imbibition plots log time (min) vs. log cumulative imbibition (mm) have generally have 2-3 unique slopes (Type I, II, and III slope) that represent individual imbibition stages. Type I slope (~2-4) consist of the first few seconds of initial recording occurs when the sample surface touches the fluid, relating to initial fluid/rock surface interaction. Type II slope (~0.6) records the fluid uptake onto the sample surface and is related to microfractures and/or laminations present in the sample. Type III slope referred to as the interior connectivity slope records edge-accessible and connected pore spaces of a porous medium representing of either a well-connected (~0.5) or poorly (~0.25) connected pore spaces. Slope IV (~0.1) occurs when the fluid front reaches the top of the sample (Hu et al., 2001).

Imbibition and vapor absorption were performed on the following samples listed in Table 4-8. Samples performed with DI had multiple runs and measurements slightly varied between 6hr and 24hr and an average is calculated. Type III slopes ranged from 0.241 to 0.647 for DI water and 0.261 to 1.097 for DT2 (Table 4-9). Type IV slopes were not observed in the imbibition experiments. The overall results for DI indicate that there is an intermediate to

well-connected pore spaces. Type III slopes for DT2 were higher than DI and at least doubled in some samples. This may be caused by the fluid reaching the surface of the sample more quickly than DI and may be a direct result of micro-fractures and laminations present in the samples. Figures 4-9 to 4-15 displays the graphs for imbibition runs highlighted in Table 4-8.

Table 4-8: List of imbibition and vapor absorption runs performed on samples.

Sample ID	Fluid Imbibition			Vapor Absorption		
	DI Water (6hr)	DI Water (12hr)	DI Water (24hr)	DT2 (8hr)	DI Water (72hr)	DT2 (48hr)
EGSP-7378		√	√	√	√	√
EGEP-7461	√	√		√	√	√
EGSP-7495	√		√	√	√	√
EGSP-4020		√	√	√	√	√
EGSP-4122	√	√		√	√	√
BE-248	√		√	√	√	√
BNT-8299	√		√	√	√	√
BNT-8327	√		√	√	√	√
BEC-Outcrop	√	√		√	√	√
CLO-240	√		√	√	√	√

Table 4-9: Average Type III imbibition slopes for DI and DT2 fluids samples highlighted are displayed in the subsequent figures.

Sample ID	Type III Slope DI	Type III Slope DT2
EGSP-7378	0.383	0.623
EGEP-7461	0.647	1.048
EGSP-7495	0.512	1.026
EGSP-4020	0.214	0.261
EGSP-4122	0.469	0.448
BE-248	0.355	0.663
BNT-8299	0.241	0.434
BNT-8327	0.470	1.097
BEC-Outcrop	0.389	0.891
CLO-240	0.326	0.604

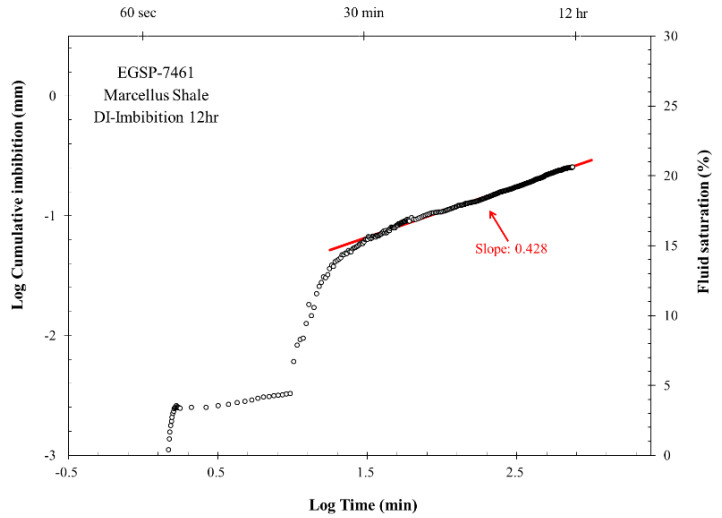

A)

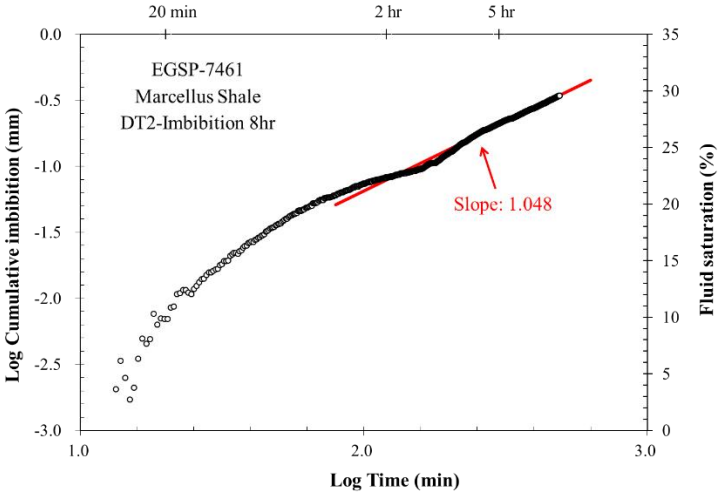

B)

Figure 4-9: Imbibition slopes of DI (A) and DT2 (B) fluids into EGSP-7461.

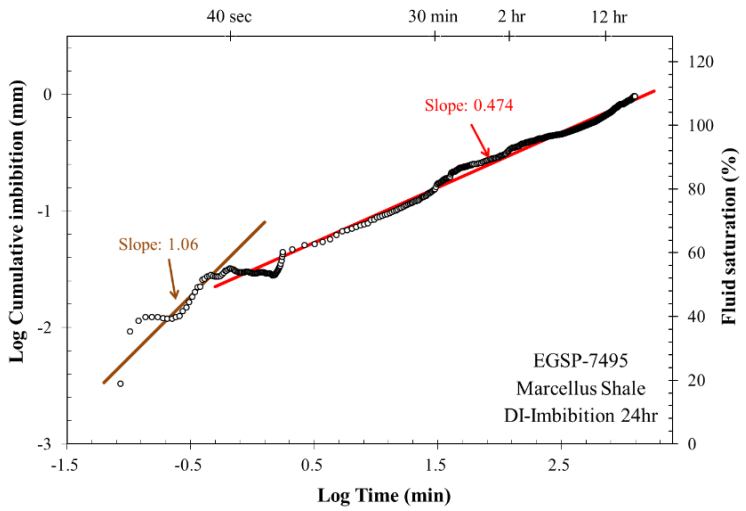

A)

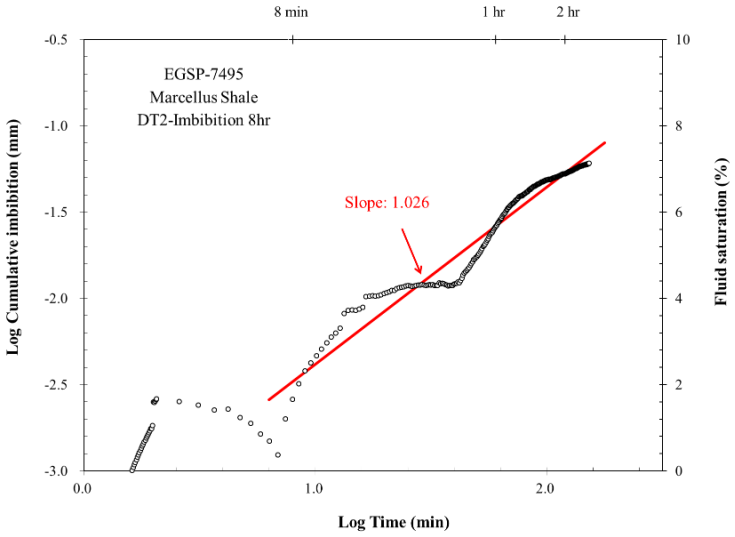

B)

Figure 4-10: Imbibition slopes of DI (A) and DT2 (B) fluids into EGSP-7495.

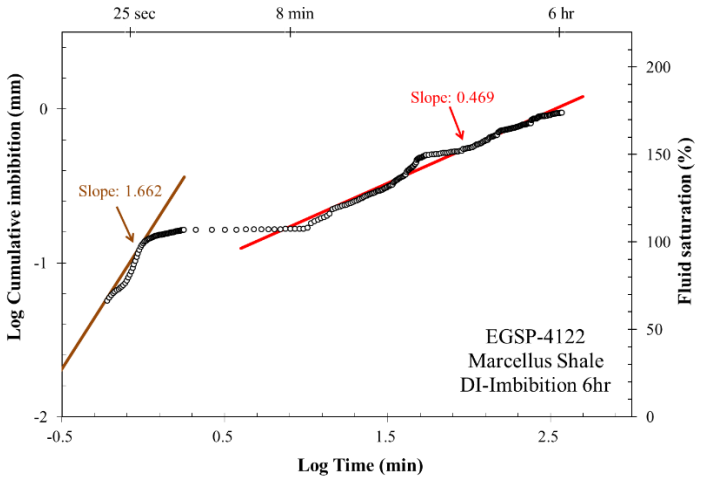

A)

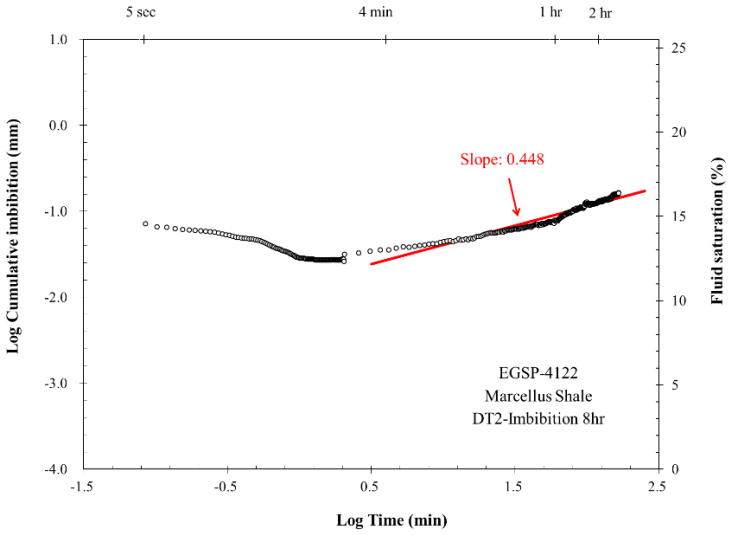

B)

Figure 4-11: Imbibition slopes of DI (A) and DT2 (B) fluids into EGSP-4122.

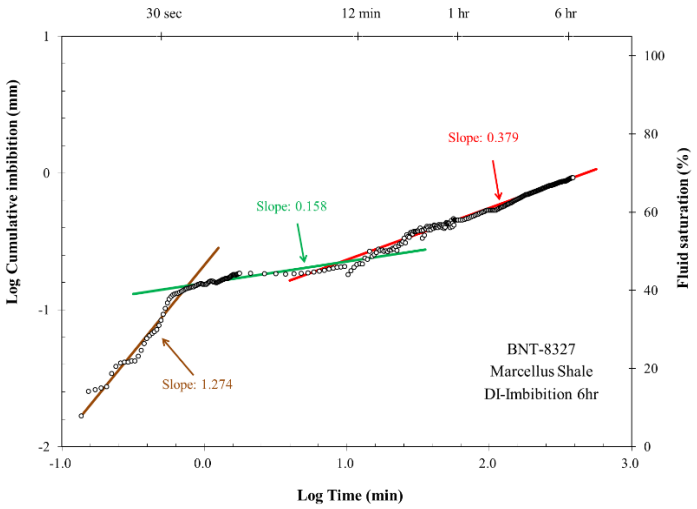

A)

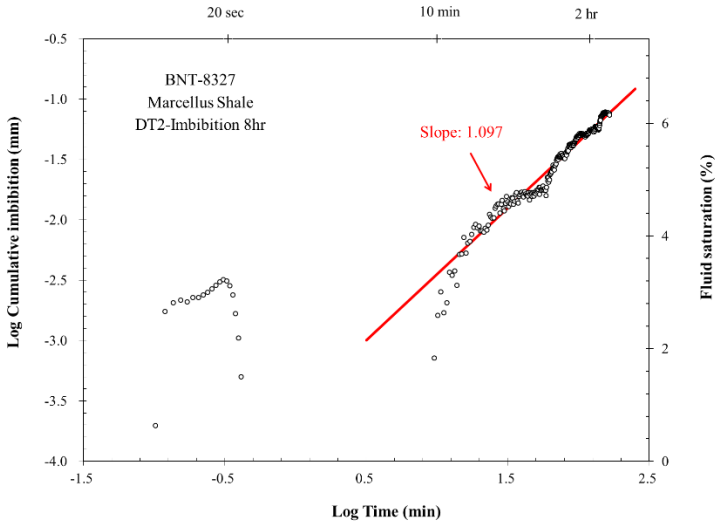

B)

Figure 4-12: Imbibition slopes of DI (A) and DT2 (B) fluids into EGSP-8327.

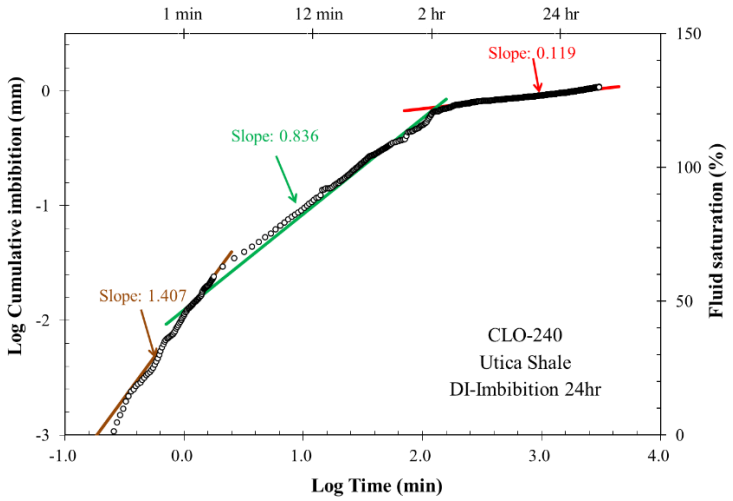

A)

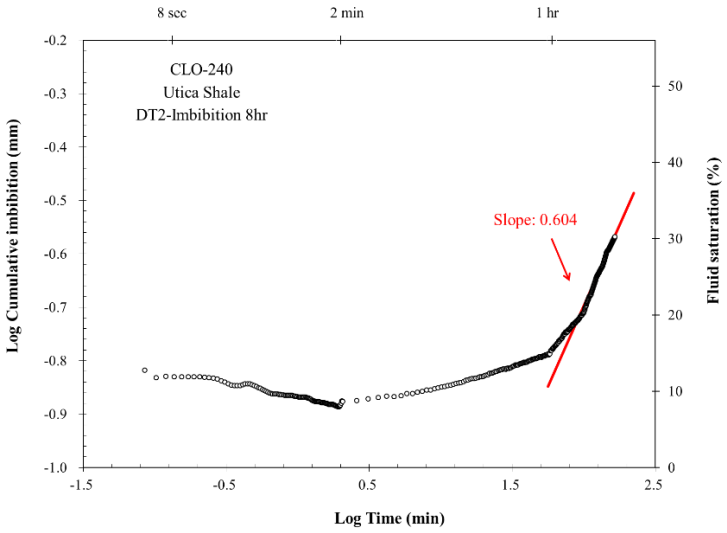

B)

Figure 4-13: Imbibition slopes of DI (A) and DT2 (B) fluids into CLO-240.

The purpose of vapor absorption is to remove the effect of surface tension that takes place in the imbibition experiments. Apparent weight gain is shown as a result of surface tension the fluid applies on a sample during imbibition runs. Vapor absorption results coincide with the contact angle measurements rather than imbibition and this may be directly resulted from surface tension weight gain. Type III slope are extremely low for BE-248 and EGSP-4020 vapor experiments suggesting that there were microfractures present, with well-connected pore spaces and the fluid reached the top of the sample surface by the end of the run. Otherwise, majority of the samples showed well-connected pore spaces with respect to water. DT2 results had much lower slopes (Table 4-10) suggesting lower pore connectivity. Figures 4-14 to 4-19 displays the graphs and slope for vapor absorption runs highlighted in Table 4-10.

Table 4-10: Type III slopes of vapor absorption tests for DI and DT2 fluids; samples highlighted are displayed in the subsequent figures.

Sample ID	Type III Slope DI	Type III Slope DT2
EGSP-7378	0.821	0.153
EGEP-7461	0.699	0.220
EGSP-7495	0.611	0.214
EGSP-4020	0.360	-
EGSP-4122	0.622	0.173
BE-248	-	0.380
BNT-8299	0.421	0.232
BNT-8327	0.548	0.294
BEC-Outcrop	0.534	0.237
CLO-240	0.512	0.347

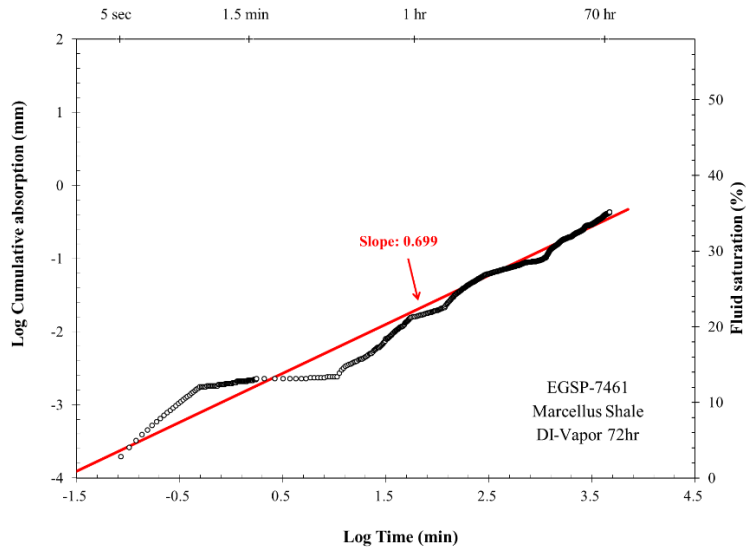

A)

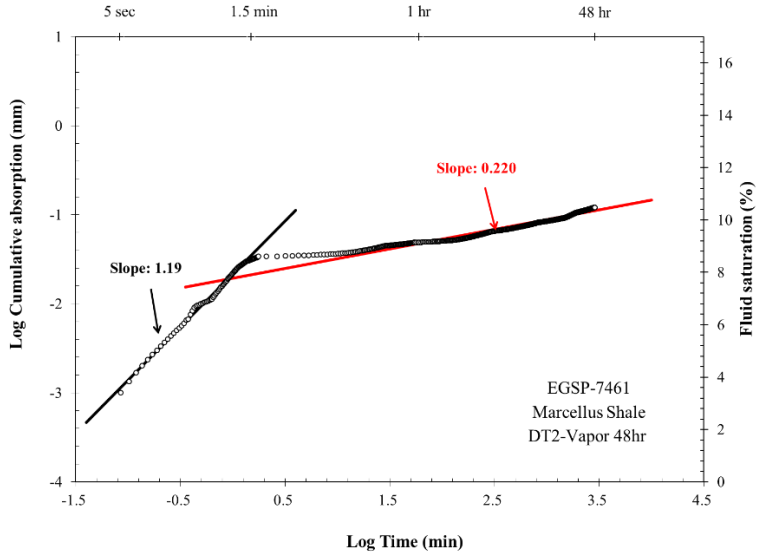

B)

Figure 4-14: Absorption slopes of DI (A) and DT2 (B) fluids into EGSP-7461.

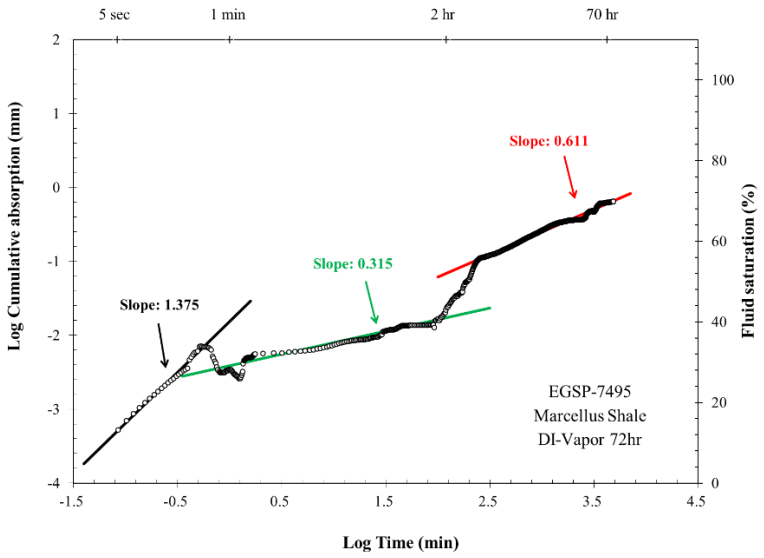

A)

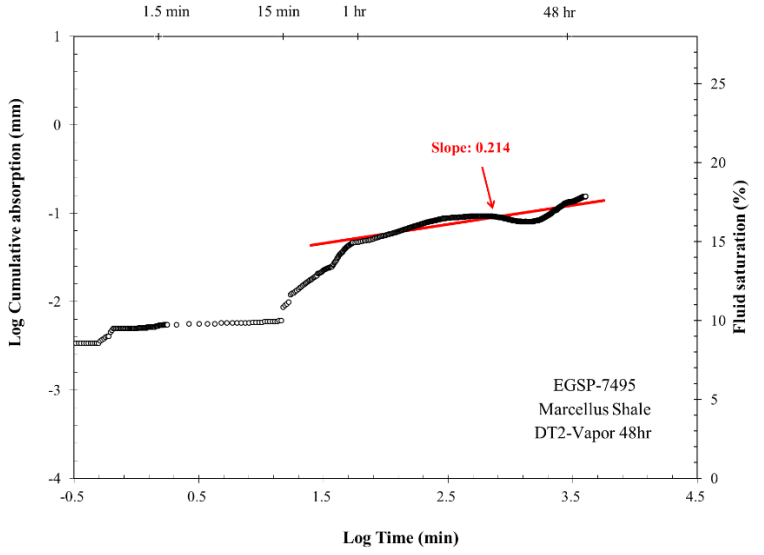

B)

Figure 4-15: Absorption slopes of DI (A) and DT2 (B) fluids into EGSP-7495.

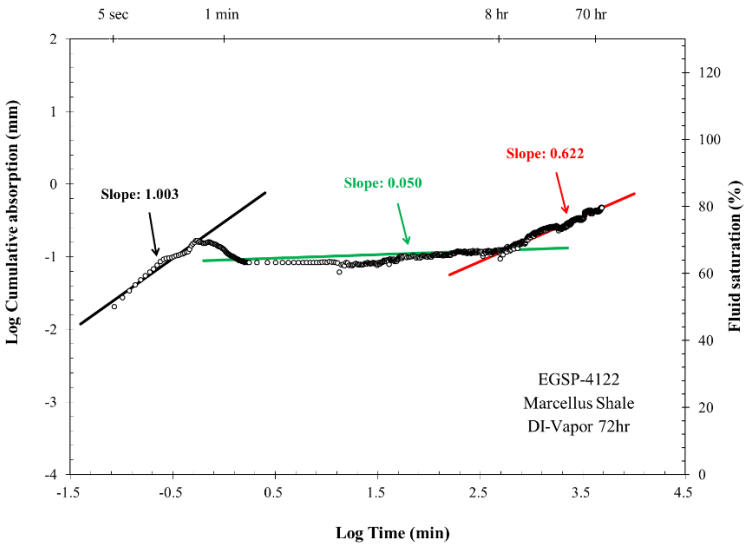

A)

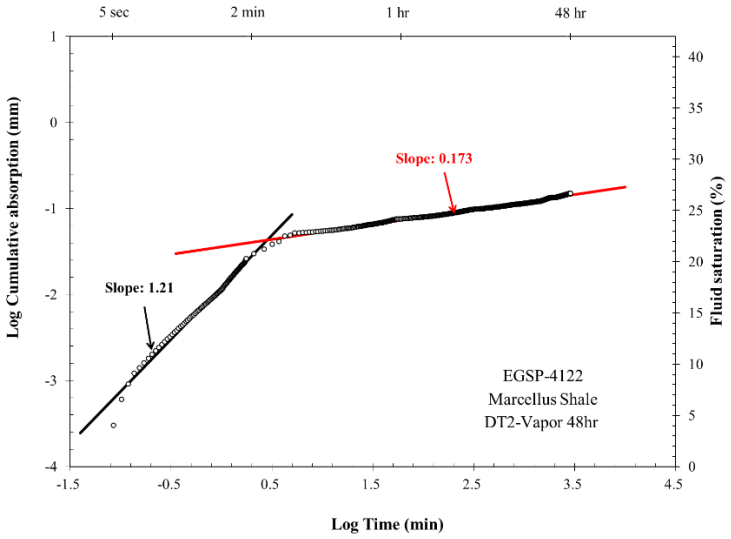

B)

Figure 4-16: Absorption slopes of DI (A) and DT2 (B) fluids into EGSP-4122.

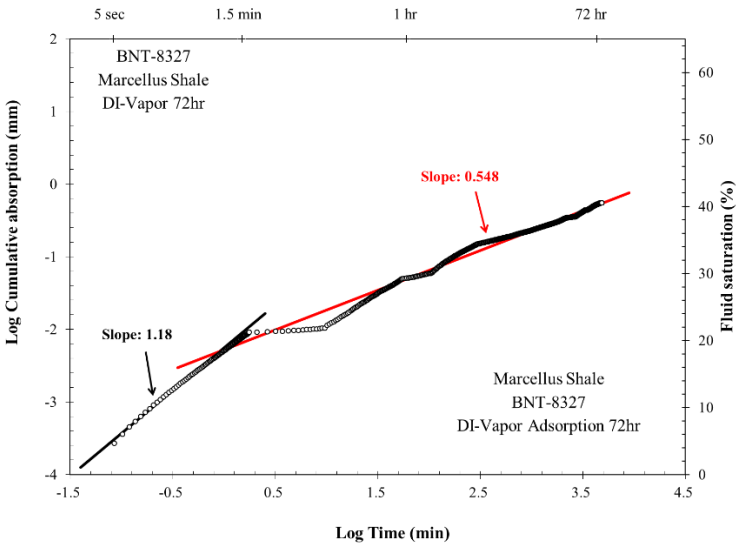

A)

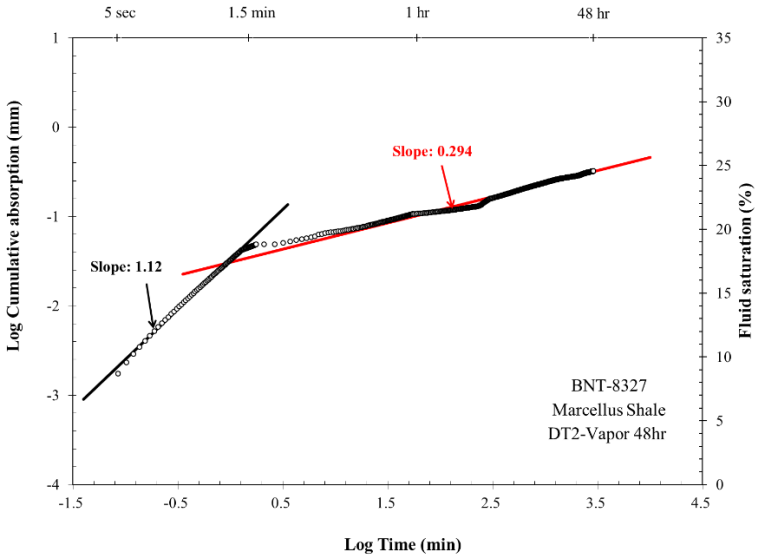

B)

Figure 4-17 Absorption slopes of DI (A) and DT2 (B) fluids into BNT-8327.

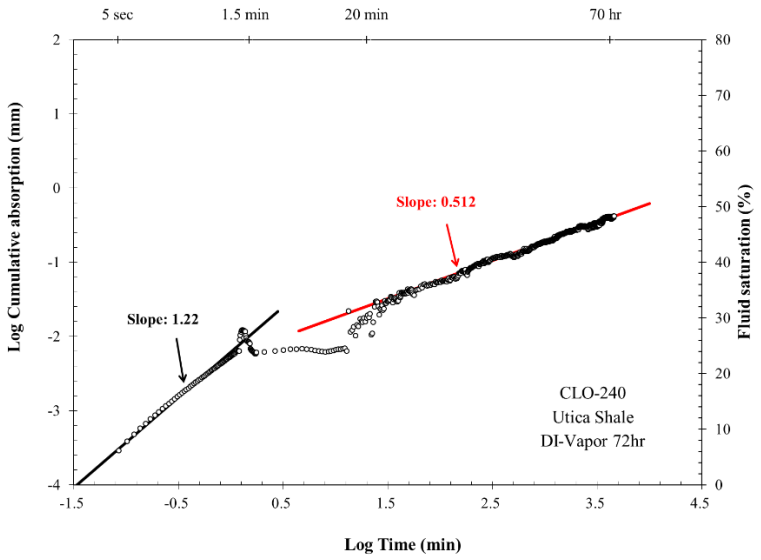

A)

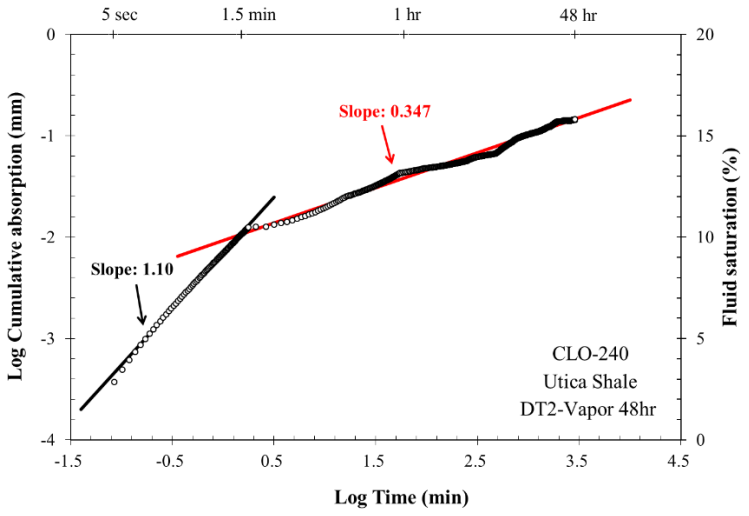

B)

Figure 4-18 Absorption slopes of DI (A) and DT2 (B) fluids into CLO-240.

4-8 Production Data

According to DrillingInfo, completion data is determined for the Bennet, EGSP-2, and EGSP-5 wells (Table 4-11). Production data were only available for the EGSP-2 well completed in 1951 with production dating back to 1982 with an initial production of 850 Mcf of gas per month (Figure 4-19) as a conventional well. Production continued and dropped to 116 Mcf in January 1985 coinciding with the national drop of 2.65-2.70 $/Mcf to 1.5-1.65 $/Mcf between 1985 to 1991. U.S total natural gas consumption decreased by 20% (EIA, 2017). Production for EGSP-2 increased from 127 Mcf at the end of 1985 to 966 Mcf in 1991. Production steadily declined from 1991 to 2008, it's unknown whether the well was perforated during its lifespan. Cumulative production was 50,921 Mcf for a duration of 108 months with a peak gas of 966 Mcf. Last date of production is 12-1-2008 and is listed as a plugged well (DrillingInfo, 2019). Only available log for Bennet (Figure 4-20) shows SP and resistivity differentiating the upper Marcellus with the Lower Marcellus by the Purcell limestone.

Table 4-11: Completion Data for Bennet, EGSP-2, and EGSP-5.

Well	Bennett	EGSP-2	EGSP-5
Completion Year	12/7/1951	5/11/1979	12/14/1979
Vertical Well	YES	YES	YES
Total Vertical Depth (TVD)	12343	7512	4702
Peforated Depth	NA	NA	3676/4130
Cumulative Oil/Gas	NA	(Gas) 50921 Mcf	NA
Status	Abandonded (Dry)	Plugged	Plugged

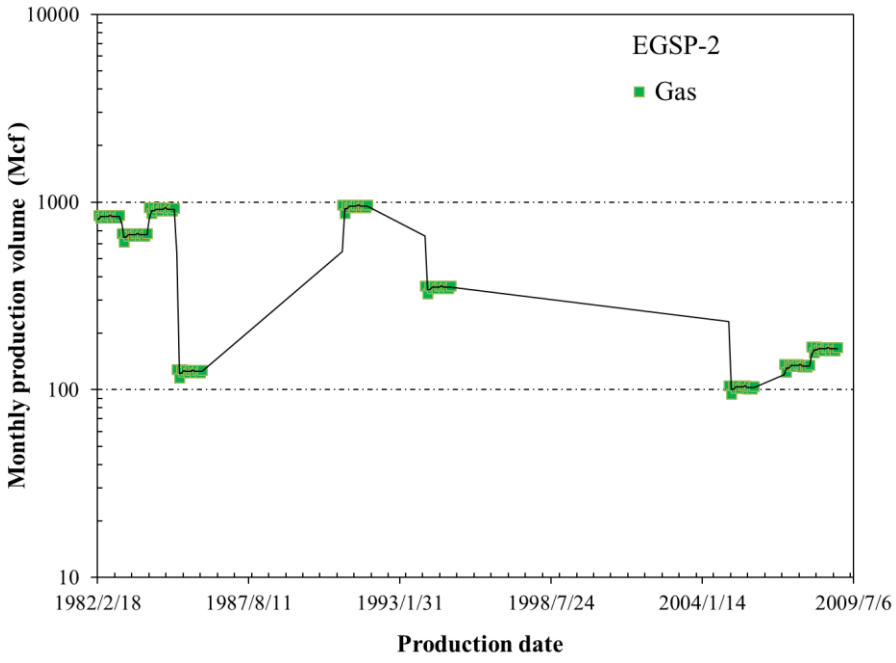

Figure 4-19: Monthly natural gas production for EGSP-2 well from 1982 to 2008. No oil and water production. (DrillingInfo, 2019).

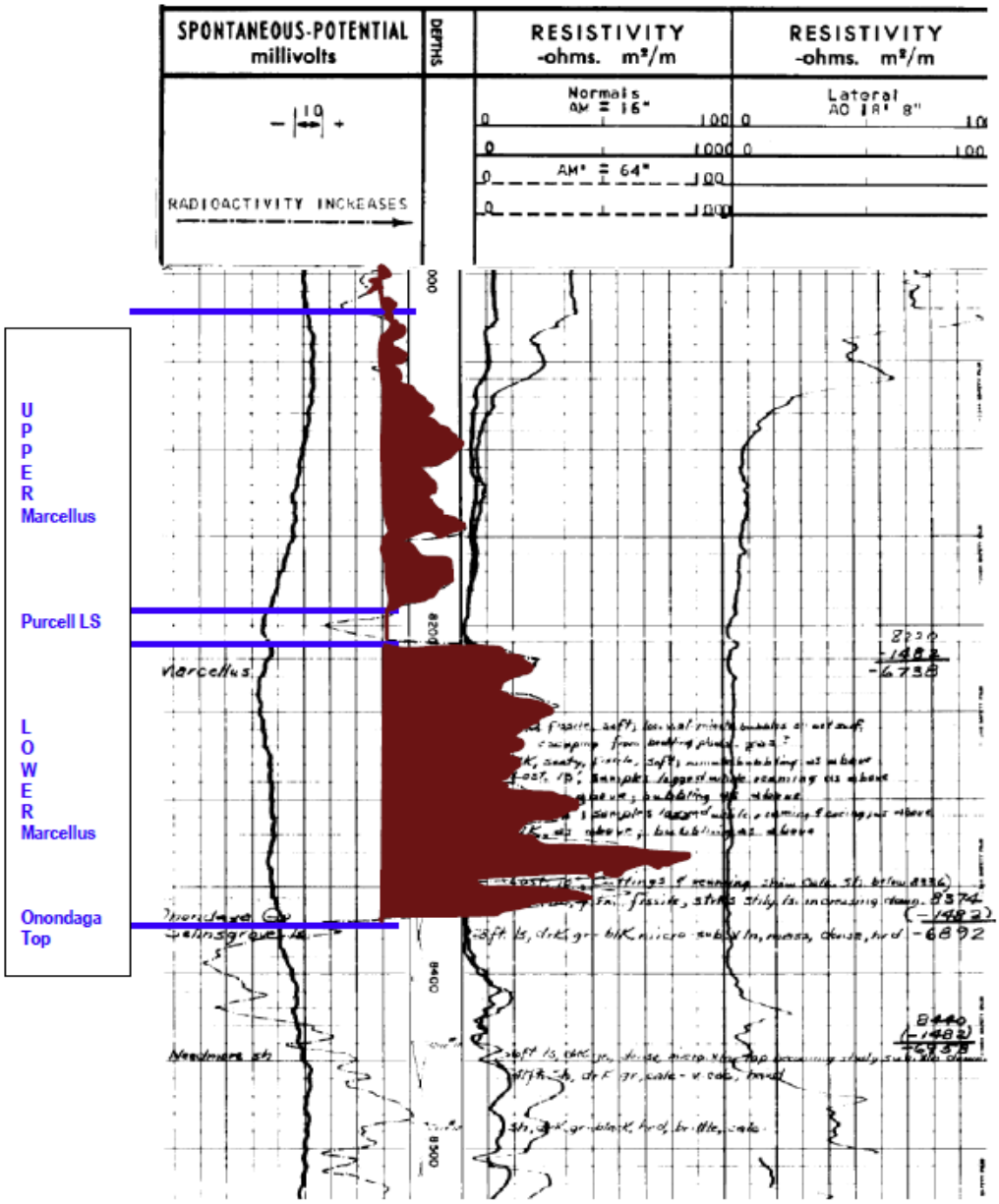

Figure 4-20: SP-Resistivity log highlighting Upper Marcellus with Lower Marcellus for Bennet well (provided by the Pennsylvania Department of Conservation and Natural Resources).

Chapter 5 - Discussion and Conclusions

Wettability

Majority of the contact angle measurements resulted in the samples exhibit water-wet behavior except for EGSP-4122 which have neutrally to oil wet tendencies. Contact angle quantifies the wettability characteristics but doesn't determine what the reservoir may be saturated with respect to depth. Contact angle values are shown at 30 seconds for DI water, API brine, and 10% THF, with a 3-degree detection limit under one second for DT2. The results show that samples are water-wet but show characteristics of absorption of DT2 causing mixed-wet behaviors due to the presence of organic and inorganic material in the rock shown by the mineralogical data (Figure 4-3). The large percentage of clay and quartz is generally water-wet, while the organic pore network is oil-wet (Borysenko et al., 2009; Tinni, 2015. As an exception, in rocks with high TOC, organic content may appear in the mineral pore network caused by tectonic forces resulting in the pores becoming oil-wet (Schieber, 2010).

Mineralogy and Geochemistry

Based on the XRD analyses from 17 samples the Marcellus is abundant in quartz and illite (Table 4-3). Calcite, ulvospinel, pyrite, albite, muscovite, and anorthite are highlyabundant and consistent through the samples. As quartz % increases,

TOC % increases (Wang and Carr, 2013). In this study, Quartz + Feldspar (%) were plotted against TOC% displaying a positive trend of increasing quartz and feldspar content with increasing TOC (Figure 5-1A). Pyrolysis data show that the Marcellus TOC ranges from 0.51% to 12.3% for samples discussed in this study. These values fall into the same range as previous studies; TOC varies in the Marcellus formation and ranges from less than 1% to 20% (Nyahay et al., 2007). A general trend shows clay content increasing as TOC % decreases (Figure 5-1B); as quartz increases, TOC % increases (Figure 5-1C). The positive correlation between quartz and TOC indicates potential for better connectivity in inorganic material.

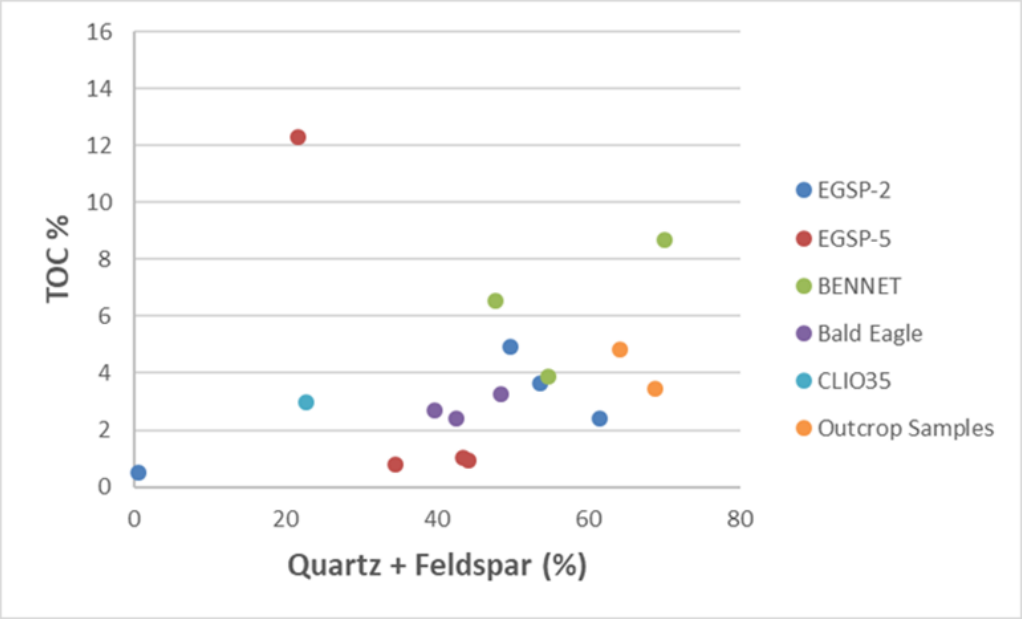

Figure 5-1: (A) Quartz + Feldspar % vs. TOC %

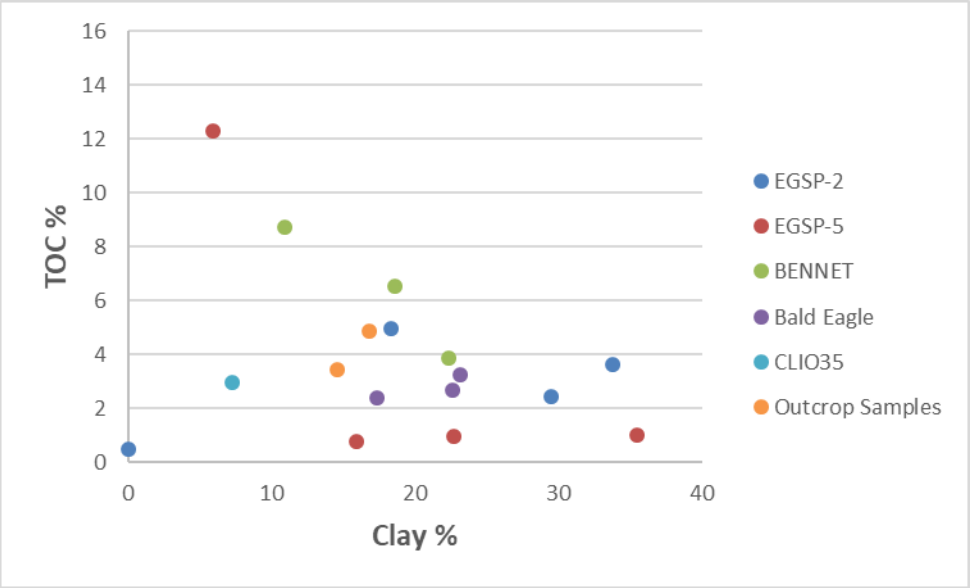

B.

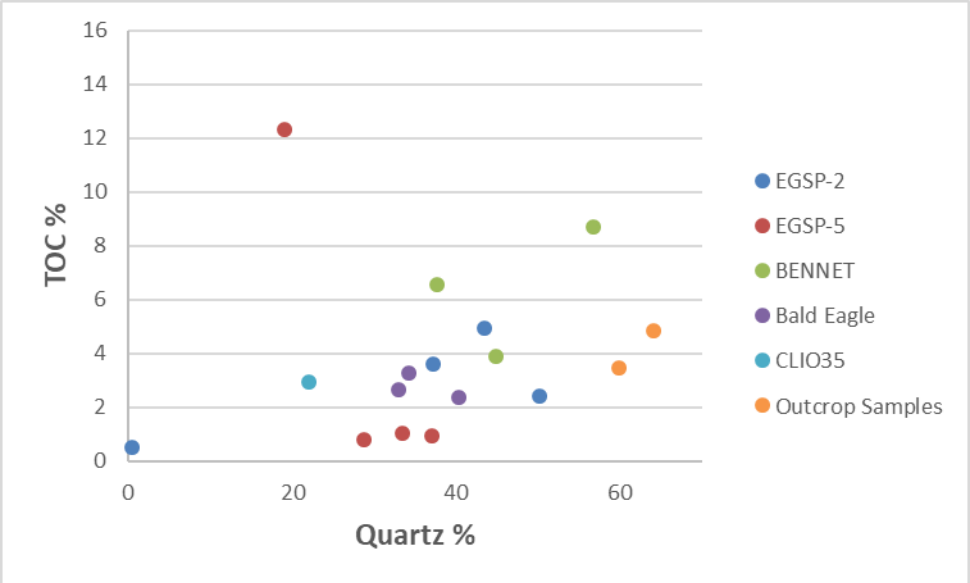

C.

Figure 5-1: (A) Quartz + Feldspar % vs. TOC %. (B) Clay % vs. TOC % (C) Quartz % vs. TOC %.

Porosity values obtained from MICP results were plotted against quartz and clay percentages show a positive correlation (Figure 5-2). This coincides with the abundance of interparticle and intraparticle pore size distribution found in the MICP analyses (Table 4-6).

Sample EGSP-4122 consists of high quartz and carbonate with low clay content has 31.3% of 0.005-0.1 µm pore-throats with 3.03% porosity resulting in potential connectivity of higher permeability rates. The edge-accessible porosity is 7.37%. This sample is part of the EGSP-5 well that was plugged with no available log or production data. From pyrolysis data EGSP-4122 has 12.3% TOC with type II kerogen content including 0.79% 10-50µm pore-throat size distribution. Once production and log data are made available and an analysis made, including data provided, this section could have potential for producing natural gas.

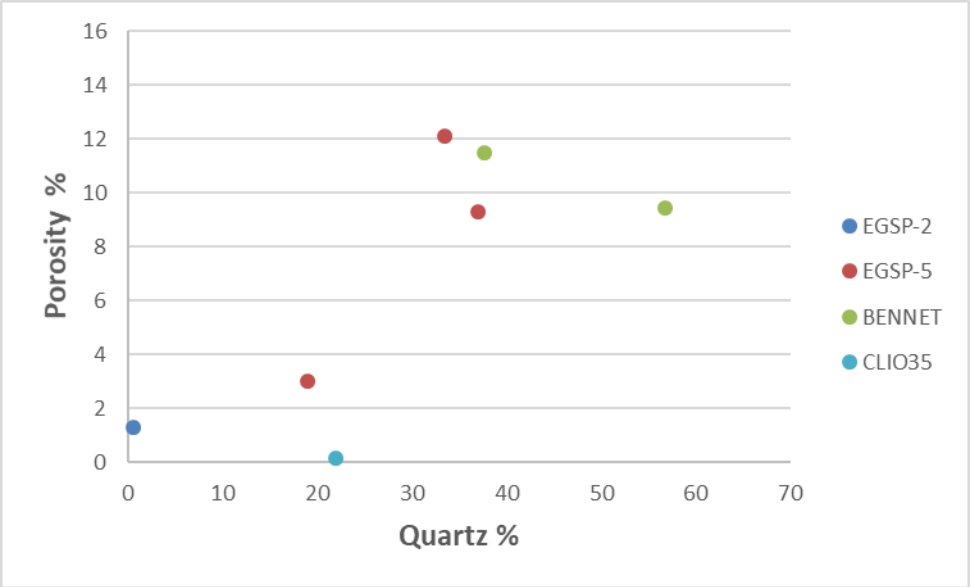

A.

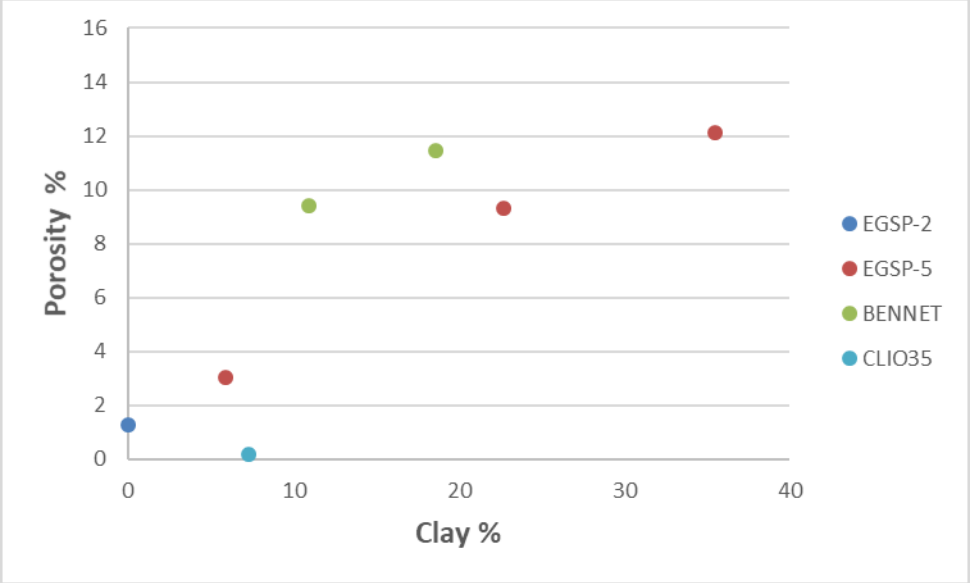

B.

Figure 5-2: Porosity vs. quartz (A) and clay (B)

Pore Structure from MICP

MICP method is used to determine pore throat distribution in porous media by mercury invasion at variable pore pressures and quantify additional petrophysical characteristics. Permeability (mD) is highest in 10-50 µm pore-throat size range with 9.75 mD concluding to the microfractures. Overall, permeability rates in this study are low and range from 7.43E-6 mD to 1.01E-5 mD in 0.0028-0.005 µm pore throats. Previous studies show that the Marcellus have wide calculated permeability ranges from 5-50 µD (Soeder et al., 1986) including ranges from 20-60 nD (Heller et al., 2014). Although results presented in this research correspond to previous studies, permeability ranges are still quite variable suggesting a complex pore network.

Majority of the samples have 10-50 µm pore-throat diameters, indicate microfractures, with relatively high interparticle to intraparticle pore-throat distribution percentages (Table 4-6 and Table 4-7). This coincides with findings of both intraparticle organic-matter hosted-pores, including intraparticle and interparticle mineral hosted pore networks (Goral, 2015) utilizing scanning electron microscopy (SEM) on cores. In addition, 0.0028-0.005 µm pore sizes are present in majority of the samples are pore spaces between clay particles that have been intruded. Porosity values calculated utilizing MICP analyses range from 1.3% to 12.1% for Marcellus samples and 0.17% for the Utica sample. These

results are similar to the 2.42%-8.3% calculated range using SEM (Goral, 2015; Gupta, 2018). It's important to note the pore-throat distribution variability for sample EGSP-7461 suggesting the complexity of the pore network. High tortuosity values coincide with the low permeable and porosity values (Table 4-7) characterize the Marcellus samples.

Vacuum saturation (Table 4-1) results were compared with liquid pycnometry (Table 4-5) and MICP (Table 4-7) in determining bulk density for the samples discussed in this study. Bulk density is important in determining kerogen content caused by low grain density values. DT2 has lower bulk density for pycnometry method because it wets both inorganic and organic pores. The MICP bulk density value for EGSP-4122 is 2.26 g/cm^3 including the 12.3% TOC contributes to the interest in this section. One of the defining characteristics of Marcellus Shale consist of having bulk densities <2.55 g/cm^3 (Boyce, 2009) in which corelates with bulk densities calculated in this study. Bulk density for the Utica averages between 2.5 to 2.7 g/cm^3, corresponds well with results shown in this study.

Pore Connectivity

Imbibition and vapor absorption experiments indicate pore connectivity that quantify the connected pore spaces as slope types (Tables 4-9 and 4-10) within tested samples. Pore connectivity is determined by the type III slope

ranging ~0.5 for well-connected to ~0.25 for poorly connected pore spaces. All samples show high values for type III imbibition slopes indicating well-connected pore spaces, except for EGSP-4122 showing poorly connected pore space in relation to DI. This concurs with the oil-wet tendencies from the sample's contact angle measurements. For imbibition type III slopes range from 0.214 to 0.647 for DI and 0.261 to 1.097 for DT2. Vapor absorption ranges from 0.360 to 0.821 for DI and 0.153 to 0.380 for DT2. One can argue that results vary depending on the mineralogy causing the fluid to imbibe or absorb onto the sample's surface. Imbibition's higher connectivity slopes may be caused by the contact of the fluid onto the sample's surface at higher values due to existing microfractures. This concludes to the vapor absorption results having lower connectivity values since the sample is suspended directly above the fluid rather than having contact.

Conclusion

The purpose of this study is to evaluate the nano-petrophysical characteristics of different zones of the Marcellus in Pennsylvania. Conclusion from the nano-petrophysical methods performed for this study are as follows:

- Samples are water-wet but show characteristics of absorption of THF and DT2 causing mixed-wet behaviors due to the presence of organic and inorganic material in the rock shown by the mineralogical data.
- Marcellus TOC ranges from 0.51% to 12.3%.

- Quartz + Feldspar (%) were plotted vs. TOC% revealing a positive trend of increasing quartz and feldspar content with increasing TOC, indicating potential for better connectivity in inorganic material.
- Majority of the samples have 10-50 μm pore-throat diameters with relatively high interparticle to intraparticle pore-throat distributions.
- Overall, permeability rates are low and range from 7.43 nD to 10.1 nD in 2.8-5 nm pore-throats.
- Porosity values calculated utilizing MICP analyses range from 1.3% to 12.1% for Marcellus samples and 0.17% for the Utica sample.
    - Increasing porosity % positively corelates with increasing TOC %.
    - A general trend shows clay content increasing as TOC % decreases.
- All samples show high values for type III imbibition slopes indicating well-connected pore spaces, except for EGSP-4020 showing poorly connected pore space in relation to DI.
- Bulk density for the Marcellus averages between 2.1 g/cm^3 to 2.6 g/cm^3 with the Utica averaging between 2.5 g/cm^3 to 2.7 g/cm^3. Pycnometry using DT2 has lower bulk density values determined by wetting of both inorganic and organic pore types.

5.1 Recommendations

It's apparent that the variability of pore-throat distribution sizes presented by MICP analyses display a complex pore network that make up the Marcellus. Results of this study will contribute to the understanding of reservoir characterization, but additional work should be conducted on understanding the micro to nanopores in tight shales. Additional analyses should be performed on different wells across different sections of the Marcellus particularly in Pennsylvania. Majority of the samples performed in this study were taken from sections at the Acadian orogeny front. Additional sampling away from the orogeny front will help contribute to studying pore networks, fluid flow, and migration of hydrocarbons of tight shales. Other petrophysical techniques such as Nuclear Magnetic Resonance (NMR), N_2 adsorption isotherm and hysteresis, Small Angle Neutron Scattering (SANS), and gas diffusion analyses in concurrence with well log analyses and production data should be performed for further contribution of reservoir characterization.

Appendix A

Laboratory Methods at Shimadzu Institute

MaximaX XRD-7000: Shimadzu X-ray Diffractometer

Sample Preparation

- Prepare your sample by compacting the sample into the sample holder using a glass slide
- Avoid vertical loading by removing excess sample with the edge of the glass slide
- Attempt to make your sample as flat and homogenous as possible; once this is completed your sample is ready to be analyzed.

Power Operations

- Turn the chiller on by pressing the power button (on the face of the chiller), a green light will illuminate.
    - Allow the chiller to sit for ~20 minutes to adjust to the proper temperature.
- Turn the XRD on by pressing the power button on the left hand side. The green power button will illuminate on the front panel of the XRD.

XRD Calibration**:**

- Locate and open the [PCXRD] program on the desktop. The main "XRD-6100/7000" panel will display.
- Click the [Display and Setup] icon, a "door alarm check" window will pop up. Follow the prompt to open and close the XRD door, once complete click "Close". An "IOcon" window will pop up with the message "Now Calibration! If ready OK", Click "OK".
- The XRD is officially calibrated and ready to process your sample.

Setting Analysis Conditions**:**

- To set the processing conditions go to the "XRD 6100/7000" panel.
- Click on the [Right Gonio Condition] icon to open the [Analysis Condition Edit Program] window
- Click the blue bar under [Measurement Mode: Standard] to open the [Standard Condition Edit] window.
- Most of the settings in the [Standard Condition Edit] window will be preset. Only a few conditions will need to be changed.
- The following general condition settings will work for a wide array of materials. *It's very important to follow these next steps, double check any settings you change ensuring to follow these guidelines precisely. This will minimize minor mistakes when processing materials and will prevent damage to the detector*.

- Scanning condition: Scan Range (deg) = 2°-70° □ Optional Condition: Check the box [Option Enable]
- Beta Attachment: Control Mode: Rotation
  Rotation Speed (rpm): 6

- Slit Condition: Slit Conditions are preset, and must be verified on the XRD to ensure the proper slit sizes match the settings listed under the Slit Conditions.
  - Checking the Slits:
    - Open the XRD door, on the left side of the XRD is the X-ray tube, the Divergence Slit is attached to the left side of the divergence soller slits.
    - On the right hand side will be the detector arm which contains a set of Scattering soller slits, the Scattering Slit faces the sample (Left) and the Receiving Slit faces the detector (Right).
    - If they are not the same sizes as what is preset in the [Slit Condition] box change the slit's so they do match.
  - Standard Slit Settings:
    - Divergence Slit: 1.0°
    - Scattering Slit: 1.0°
    - Receiving Slit: 0.3 mm

- Double check your settings and make sure they are correct, if they are click [OK].
- A [File & Sample Condition Edit] window will display; change the [Group name] to match your destination folder name and change [File name] and [Sample Name] to match your sample name, click [New].
  - Later samples can be created by simply changing the file and sample names and clicking [Modify].
- Click [Close] on the [Standard Condition Edit] window.

Starting the XRD Processing**:**

- Locate and click the [Right Giono Analysis] icon on the [XRD-6100/7000] panel.
- Your current sample name should appear highlighted blue in the upper portion of the [Right Gonio System: AnalysisCondition Edit Program] window. Highlight your sample and click [Append], this adds your sample to the list in the bottom portion of the window labeled [Entry for Analysis], click [Start]. Your sample should appear in the bottom of the [Right Giono Analysis & Spooler Program] window, click [Start] in this window. This officially starts the analysis process.
  - Indicators for Analysis: A clicking sound will come from the XRD when the locking mechanism on sliding door locks. On the face of the XRD a yellow light should illuminate under [X-RAYS ON].

- Leave all software windows open and allow the XRD to process your sample, this should take ~30 minutes.

Completed XRD Processing**:**

- A complete peak spectrum should appear in the [Right Giono Analysis & Spooler Program] window upon completion.
- The green [Analyzing!] Box should disappear and the yellow [X-RAYS ON] light should turn off.
- If you have more samples to analyze, continue to run your samples in the same manner listed above.

Opening Peak Profile Spectrum**:**

- Locate and open the icon for the [MDI jade 9] software on the Desktop.
- Under [file], click [Read], locate the folder [xddat] under [favorites]. Locate the folder where your samples are saved.
- In your folder, each sample should have a [.RAW] file, use this file to open your selected spectrum in the [Jade 9] software.

Identifying Minerals in Peak Spectrum**:**

It's important to have an educated background on the sample you're analyzing. Knowledge regarding the bulk composition and what you're searching for will greatly reduce the amount of time spent IDing the various peaks in the spectrum.

- Locate the [Find Peaks] icon on the main tool bar next to the [Floppy Disk/Save] icon, this will identify and mark any statistically significant peaks within the spectrum
- Choose a mineral database: At the top of the panel to the right of the spectrum window, there will be a drop down menu choose the [RDB-Minerals] as the database. The RDB-Mineral database should be predominately used to identify most minerals in your spectra.
    - If you cannot find a mineral in the RDB-Minerals database change to the [PDF+4 Minerals] database library, but be sure to change back to the RDB database once the mineral is located.
- Begin searching for minerals based on your pre-existing knowledge regarding the sample. When you identify minerals that fit your peak spectrum hit [Enter] on the keyboard, this process will add the minerals to a compiled list of those minerals which you identified in the spectrum.

- Once you have exhausted your initial hypothetical list of minerals, a helpful tool to use is the [Line Based Search/Match]. Go to the main tool bar and locate [Identify] and select the [Line Based Search] option.
    - This tool will compile a list of minerals by searching a selected PDF database for entries with peaks which are statistical matches for the peaks identified within your spectrum.
    - Settings:
        - [Two-Theta Error Window] max setting should be no more than 0.24%
        - [Top Hits to List] max setting 80
    - Set the parameters and click the blue [Play] icon next to the [X] to run the search and generate a list of possible phases that might fit your spectra. *Note: the line based search should not be used as a primary way to identify the bulk mineral mode of the sample as the software is not consistent when generating phases and will possibly leave out important phases for the spectrum*.

Model Analysis**:**

- Once all minerals have been ID'd, check that they have been added to the mineral list by pushing [Enter] on the keyboard.
- Click the [%] icon next to the drop-down mineral list located on the toolbar in the middle of the window to begin modal analysis.
    - An overlay will appear with different chart configurations of the modal results, to change the configurations of the chart use the drop down menu in the chart window.
- To view the modal analysis in text format: locate and click the […] icon near the [%] icon. This will list the minerals by name, chemical formula, and the normalized weight percent for each mineral. It will also state if the mineral is a [major], [minor], [trace], or [absent] component in the sample.
- If you would like to remove a mineral from your mineral list at any time, highlight the mineral and press [Delete] on the keyboard. [Absent] phases should be removed from the list by this method.

Analysis Check with Pattern Deconvolution**:**

- A key indication that the peak spectrum has been fully fitted and identified is by using the [Pattern Deconvolution] tool which automatically runs with the modal analysis.
    - The pattern deconvolution tool will generate a red overlay spectrum on top of the original white spectrum.

    - This process is generating a [Best Fit Profile] composed of the selected mineral standards from the [Mineral PDF database library] with your sample spectrum.
    - If all minerals have been properly identified, then the red deconvolution overlay will match the peak spectra for each peak. If there are peaks that don't have the red deconvolution overlay then those peaks have not been identified.
- Continue processing your spectrum until your original spectra and the deconvolution spectra match.

Saving Data**:**

To save your data,

- Go to [file] and [Save], save your data under [Current work as *.SAV]. This will save all analysis as a separate file.

Appendix B

Laboratory Methods at GeoMark

1. Sample Requirements for a Typical Geochemical Program

For geochemical analysis a teaspoon (ca. 10 g.) of sample material is needed when TOC, Rock-Eval, vitrinite reflectance and residual hydrocarbon fluid fingerprinting is to be completed. If possible, a tablespoon is preferred. However, it is possible to complete a detailed program with even less sample, although there is dependency on the sample characteristics (e.g., organic richness, abundance of vitrinite, amount of staining). Sample prep includes grinding the sample with mortar and pestle until it passes through a 60 mesh sieve.

2. Total Organic Carbon (TOC) – LECO C230 instrument

Leco TOC analysis requires decarbonation of the rock sample by treatment with hydrochloric acid (HCl). This is done by treating the samples with Concentrated HCL for at least two hours. The samples are then rinsed with water and flushed through a filtration apparatus to remove the acid. The filter is then removed, placed into a LECO crucible and dried in a low temperature oven (110 C) for a minimum of 4 hours. Samples may also be weighed after this process in order to obtain a % Carbonate value based on weight loss.

The LECO C230 instrument is calibrated with standards having known carbon contents. This is completed by combustion of these standards by heating to 1200^{o}C in the presence of oxygen. Both carbon monoxide and carbon dioxide are generated, and the carbon monoxide is converted to carbon dioxide by a catalyst. The carbon dioxide is measured by an IR cell. Combustion of unknowns is then completed and the response of unknowns per mass unit is compared to that of the calibration standard, thereby the TOC is determined.

Standards are analyzed as unknowns every 10 samples to check the variation and calibration of the analysis. Random and selected reruns are done to verify the data. The acceptable standard deviation for TOC is 3% variation from established value.

3. Rock Eval / HAWK Pyrolysis
Approximately 100 milligrams of washed, ground (60 mesh) whole rock sample is analyzed in the Rock-Eval or HAWK instrument. Organic rich samples are analyzed at reduced weights whenever the S2 value exceeds 40.0 mg/g or TOC exceeds 7-8%. Samples must be re-analyzed at lower weights when these values are obtained at 100 mg.

RE-II Operating Conditions

S1: 300^{o}C for 3 minutes
S2: 300^{o}C to 550^{o}C at 25^{o}C/min;
hold at 550^{o}C for 1 minute

S3: trapped between 300 to 390^{o}

RE-VI Operating Conditions

S1: 300^{o}C for 3 minutes
S2: 300^{o}C to 650^{o}C at 25^{o}C/min;
hold at 650^{o}C for 0 minute
S3: measured between 300 to 400^{o}

HAWK Operating Conditions

S1: 300^{o}C for 3 minutes
S2: 300^{o}C to 650^{o}C at 25^{o}C/min;
hold at 650^{o}C for 0 minute
S3: measured between 300 to 400^{o}

Measurements from Rock-Eval are:

S1: free oil content (mg HC/g rock)
S2: remaining generation potential (mg HC/g rock)
T_{max}: temperature at maximum evolution of S2 hydrocarbons (^{o}C)
S3: organic carbon dioxide yield (mg CO_2/ g rock)

Several useful ratios are also utilized from Rock-Eval and TOC data. These are:

Hydrogen Index (HI):	S2/TOC x 100 (in mg HC/g TOC)
Oxygen Index (OI):	S3/TOC x 100 (in mg CO_2/g TOC)
Normalized Oil Content:	S1/TOC x 100 (in mg HC/g TOC)
S2/S3:	
Production Index (PI):	S1/ (S1+S2)

Instrument calibration is achieved using a rock standard. Its values were determined from a calibration curve to pure hydrocarbons of varying concentrations. This standard is analyzed every 10 samples as an unknown to check the instrument calibration. If the analysis of the standard ran as an unknown does not meet specifications, those preceding data are rejected, the instrument recalibrated, and the samples analyzed again. However, normal variations in the standard are used to adjust any variation in the calibration response. The standard deviation is considered acceptable under the following guidelines:

T_{max}: $\pm 2^{o}C$
S1: 10% variation from established value
S2: 10% variation from established value
S3: 20% variation from established value

Analytical data are checked selectively and randomly. Selected and random checks are completed on approximately 10% of the samples. A standard is analyzed as an unknown every 10 samples.

4. Turnaround Time:

The standard turnaround time for sample orders over the past 12 months is approximately 2 to 3 weeks, depending on number of samples in the order.

References

Agbalaka C., Dandekar, A.Y., Patil, S.L., Khataniar, S., Hemsath, J.R., 2008, The effect of wettability on oil recovery: A review, Paper presented at the SPE Asia Pacific Oil and Gas Conference and Exhibition 2008 – "Gas Now: Delivering on Expectations;" Perth, Western Australia, Australia, 1, p. 73-85.

Barnes, J.H., and Sevon, W.D., 2014, The geological story of Pennsylvania (4th ed.): Pennsylvania Geological. Survey, 4th Ser., Educational Series 4, p. 44.

Belvalkar, R.A., and Oyewole, S., 2010, Development of Marcellus Shale in Pennsylvania. Society of Petroleum Engineers. doi:10.2118/134852-MS.

Blakey, R., 2011, Middle Devonian (385Ma), North American Paleogeogprahy: http://jan.ucc.nau.edu/rcb7/nam.html (accessed on March 18, 2019).

Borysenko, A., Clennell, B., Burgar, I., Dewhurst, D., Sedev, R., and Ralston, J., 2009, Application of low field and solid-state NMR spectroscopy to study the liquid/liquid interface in porous space of clay minerals and shales. Diffusion-Fundamentals, 10, 2.1–2.4.

Boyce, M., Carr, T., 2009, Lithostratigraphy and Petrophysics of the Devonian Marcellus Interval in West Virginia and Southwestern Pennsylvania. Unconventional Energy Resources: Making the Unconventional Conventional: 29th Annual GCSSEPM Foundation Bob F. Perkins Research Conference. 10.5724/gcs.09.29.0254.

Crowe, C.W., 1969, Method of lessening the inhibitory effects to fluid flow due to the presence of solid organic substances in a subterranean formation.

de Witt, W., Jr., 1993, Principal oil and gas plays in the Appalachian Basin (Province 131): U.S. Geological Survey Bulletin 1839-I, 37 p.

de Witt, W., Jr., Roen, J.B., and Wallace, L.G., 1993, Stratigraphy of Devonian black shales and associated rocks in the Appalachian basin, in Roen, J.B., and Kepferle, R.C., 1993, Petroleum geology of the Devonian and Mississippian black shale of eastern North America: U.S. Geological Survey Bulletin 1909B, p. B1-B57.

EIA (Energy Information Administration)., 2017, Marcellus Shale Play Geology Review. https://www.eia.gov/maps/pdf/MarcellusPlayUpdate_Jan2017.pdf (accessed on January 15, 2019).

EIA (Energy Information Administration)., 2017, Natural Gas Weekly Update. https://www.eia.gov/naturalgas/weekly/archivenew_ngwu/2017/11_02/#itn-tabs-0 (accessed on January 15, 2019).

Ettensohn, F., 1985, The Catskill Delta complex and the Acadian Orogeny: A model. 10.1130/SPE201, p. 39.

Ettensohn, F.R., 2008, The Appalachian Foreland Basin in Eastern United States. *In*: MIALL, A.D. (ed.), The Sedimentary Basins of The United States and Canada. Sedimentary Basins of the World, 5. Elsevier, p. 105-179.

Flint, A.L. and L. E. Flint, 2002, "Particle Density," In: J. H. Dane and G. C. Topp, Eds., Methods of Soil Analysis, Part (4), Physical Methods, 3rd Edition, SSSA, Madison, pp. 229-241.

Gao, Z., and Hu, Q., 2012, Using spontaneous water imbibition to measure the effective permeability of building materials. Special Topics & Reviews in Porous Media: An International Journal, v. 3, p. 209.

Gao, Z., and Hu, Q., 2013, Estimating permeability using median pore-throat radius obtained from mercury intrusion porosimetry. Journal of Geophysics and Engineering, v. 10, p. 025014.

Goral, J., Miskovic, I., Gelb, J., and Kasahara, J., 2015, Pore network investigation in Marcellus Shale rock matrix. Society of Petroleum Engineers. doi:10.2118/176988-MS

Gupta, I., Jernigen, J., Curtis, M., Rai, C., and Sondergeld, C., 2018, Water-wet or oil-wet: is it really that simple in shales?, SPWLA-2018-v59n3a2, Society of Petrophysicists and Well-Log Analysts.

Harper, J.A., 1999, Chapter 7: Devonian, in Shultz, C.H., ed., 1999, The geology of Pennsylvania: Pennsylvania Bureau of Topographic & Geologic Survey and Pittsburgh Geological Society, p. 108-127.

Harper, J. A., 2008, Pennsylvania Geology, v.38, no. 1, p. 2-13.

Hu, Q., Persoff, P., and Wang, J.S., 2001, Laboratory measurement of water imbibition into low-permeability welded tuff. Journal of Hydrology, v. 242, p. 64-78.

Hu, Q., Ewing, R.P., and Dultz, S., 2012, Low pore connectivity in natural rock. Journal of Contaminant Hydrology, v. 133, p. 76-83, doi: 10.1016/j.jconhyd.2012.03.006.

Hu, Q., Ewing, R.P., and Rowe, H.D., 2015a, Low nanopore connectivity limits gas production in Barnett formation. Journal of Geophysical Research: Solid Earth, v. 120, p. 8073-8087.

Heller, R., Vermylen, J., and Zoback, M., 2014., Experimental investigation of matrix permeability of gas shales. Experimental investigation of matrix permeability of gas shales. AAPG Bulletin, *98*(5), 975-995.

Katz, A., and Thompson, A., 1987, Prediction of rock electrical conductivity from mercury injection measurements. Journal of Geophysical Research: Solid Earth, v. 92, p. 599-607.

Lash, G.G., and Engelder T., 2011, Thickness trends and sequence stratigraphy pf the Middle Devonian Marcellus Formation, Appalachian basin: implications for Acadian foreland basin evolution. AAPG Bulletin, 95:61-103.

Lee, D.S., Herman, J.D., Elsworth, D., 2011, A critical evaluation of unconventional gas recovery from the Marcellus shale, northeastern United States, KSCE Journal of Civil Engineering 15(4): p. 679-687

Male, F., Marder, M. P., Browning, J., Ikonnikova, S., and Patzek, T., 2016., Marcellus Wells' ultimate production accurately predicted from initial production. Society of Petroleum Engineers. doi:10.2118/180234-MS

Marcellus Shale Coalition. Information on Shale Gas. http://marcelluscoalition.org/pa-map/

Nyahay, R., Leone, J., Smith, L., Martin, J., and Jarvie, D., 2007, Update on regional assessment of gas potential in the Devonian Marcellus and Ordovician Utica shales of New York: Search and Discovery Article 10136

Pommer, M., and K. Milliken., 2015, Pore types and pore-size distributions across thermal maturity, Eagle Ford Formation, southern Texas. AAPG Bulletin, 99(9): 1713-1744.

Rezaee, R., Fundamentals of Gas Shale Reservoirs., 2015, John Wiley & Sons, Hoboken, New Jersey, USA, 456 pp.

Schieber, J., 2010, Common themes in the formation and preservation of intrinsic porosity in shales and mudstones— Illustrated with examples across the Phanerozoic, Paper SPE-132370 presented at the SPE Unconventional Gas Conference, Pittsburg, Pennsylvania, USA, 23–25 February. DOI: 10.2118/132370-MS.

Soeder, D., Randolph, P.L., and Matthews, R.D., 1986, Porosity and permeability of eastern Devonian gas shale. Topical Report DOE/MC/20342-8 prepared for U.S. Department of Energy under contract DE-AC21-83MC20342.

Shultz, C.H., ed. 1999, The Geology of Pennsylvania. Special Publication, no.1., Harrisburg, Pa.: Pittsburgh, Pa.: Pennsylvania Geological Survey; Pittsburgh Geological Society.

Tinni, A., 2015, Pore Connectivity and Hydrocarbon Storage in Shale Reservoirs, unpublished PhD Dissertation, University of Oklahoma, Norman, Oklahoma.

U.S. Energy Information Administration (EIA). Annual Energy Outlook 2013; Washington, DC, 2013.

Wang, G., and Carr, T., 2013, Organic-rich Marcellus Shale lithofacies modeling and distribution pattern analysis in the Appalachian Basin. AAPG Bulletin. 97. 2173-2205.

Wang, S., Javadpour, F., and Feng, Q., 2016, Confinement correction to mercury intrusion capillary pressure of shale nanopores. Scientific Reports, v. 6, p. 20160

Washburn, E.W., 1921, Note on a method of determining the distribution of pore sizes in a porous material. Proceedings of the National Academy of Sciences of the United States of America, v. 7, p. 115-116.